

A simplified three-dimensional shallow landslide susceptibility framework considering topography and seismicity

Abstract Shallow landslides are a prevalent concern in mountainous or hilly regions that can result in severe societal, economic, and environmental impacts. The challenge is further compounded as the size and location of a potential slide is often unknown. This study presents a generalized approach for the evaluation of regional shallow landslide susceptibility using an existing shallow landslide inventory, remote sensing data, and various geotechnical scenarios. The three-dimensional limit equilibrium model derived in this study uses a raster-based approach that uniquely integrates tree root reinforcement, earth pressure boundary forces, and pseudo-static seismic accelerations. Contributions of this methodology include the back-calculation of soil strength from a landslide inventory, sensitivity analyses regarding landslide size-pixel size relationships, and the determination of shallow landslide susceptibility for a landscape or infrastructure considering various root, water, and seismic conditions using lidar bare-earth DEMs as a topographic input. Using a distribution of inventoried landslide points and random points in non-landslide locales, the proposed methodology demonstrated reasonable correlation between regions of high landslide susceptibility and observed shallow landslides within a 150-km² region of the Oregon Coast Range when the water-height ratio was 0.5. The method may be improved by considering spatial hydrologic conditions and geology more explicitly.

Keywords Lidar · Three-dimensional slope stability · Susceptibility analysis · Infrastructure · Seismic · Shallow landslides

Introduction

Landslides are natural hazards that frequently result in major societal, economic, and environmental impacts on an international scale (Schuster 1996). Landslides often occur in conjunction with causative extreme events, such as heavy precipitation, significant seismic events, and wildfire (Petley 2012). In particular, shallow landsliding presents a persistent hazard, especially in mountainous, marginally stable regions with weak, yet critical root reinforcement (Roering et al. 2003). In seismically active areas, strong earthquake motions are also capable of destabilizing a slope that would normally be stable under static conditions (Parker et al. 2011; Barlow et al. 2015; Wang and Rathje 2015). The sizes and locations of potential landslides are often unknown, which present significant challenge to planners and engineers (Jibson et al. 2000). Inability to detect and mitigate potential landslides can result in significant losses to infrastructure and human life (Schuster 1996).

Landslide susceptibility mapping identifies regions of slope instability based on probabilities of landslide occurrence. “Hazard map” is often confused as a synonym for “susceptibility map”; however, the two should be distinguished. In particular, hazard maps are developed by considering the temporal occurrence or recurrence and magnitude of failure, and susceptibility maps consider whether

conditions would likely lead to failure (Hervás and Bobrowsky 2009). Aside from qualitative susceptibility mapping (i.e., maps developed by allowing experience and judgment to dictate the spatial limits of a hazard), two primary types of methods for creating quantitative susceptibility maps exist in practice: (1) statistical methods (Ayalew and Yamagishi 2005; Carrara et al. 1991; Dai and Lee 2002; Ohlmacher and Davis 2003; Xu et al. 2013) and (2) deterministic methods, often calibrated to statistical distributions of geotechnical inputs and landslide spatial properties (Bellugi et al. 2015; Dietrich et al. 1995; Milledge et al. 2014; Miller and Sias 1998; van Westen and Terlien 1996; Xie et al. 2006). Statistical methods typically utilize the historical links between landslide distribution and the factors controlling a landslide (e.g., slope), whereas deterministic methods for creating susceptibility maps utilize mechanical properties of the soil (e.g., density, friction angle) to express instability as a factor of safety, defined as the ratio of forces resisting failure to forces driving failure (Ayalew and Yamagishi 2005).

An integral part of effective landslide susceptibility mapping is the use of geographic information systems (GIS). Modern remote sensing techniques, such as light detection and ranging (lidar), have significantly improved the ability to capture topographic information for generating digital elevation models (DEMs) at high resolution, particularly in locales covered with vegetation (Sithole and Vosselman 2004; Jaboyedoff et al. 2012; Hopkinson et al. 2016). Derivative products, such as slope and slope direction (i.e., aspect), can be calculated for each cell of a DEM. Accordingly, lidar-derived DEMs enable the extraction of relevant topographic and geomorphic information at high resolution, which can be used to improve landslide susceptibility maps (Burns et al. 2008; Jaboyedoff et al. 2012; Umar et al. 2014; Youssef et al. 2015; Mahalingam and Olsen 2015; Mahalingam et al. 2016). A common approach in GIS raster analysis is to compute slope values by finding the maximum rate of change in elevation among neighboring cells in the DEM, which is highly dependent on resolution. Different DEM resolutions can produce different values for slope, which will ultimately yield differing estimates of landslide susceptibility (Mahalingam and Olsen 2015).

Deterministic methods for assessing shallow landsliding are usually performed using two-dimensional (2D) limit equilibrium analyses, such as the infinite slope analysis, which can employ the raster structure of DEMs (Dietrich et al. 1995; Iida 2004; Tsai and Yang 2006; van Westen and Terlien 1996; Wu and Sidle 1995). A fundamental assumption of the infinite slope analysis is that an infinitely long planar slope surface fails along a single failure plane parallel to the surface. These kinematics assume that a slope fails in translation and the landslide mass is sufficiently wide and long in comparison to depth. This assumption enables omission of boundary forces at the head, base, and sides of a slide as they may be negligible in comparison to the gravity-driven forces of the slide body. Although the infinite slope analysis is a relatively simple approach to evaluating slope stability, comparison of

results for infinite slope and finite element methods show that the infinite slope analysis only becomes suitable for modeling shallow landsliding on slopes with length to height ratios of 25 or larger (Milledge et al. 2012). In contrast, three-dimensional (3D) slope stability methods account for edge effects and yield higher factors of safety than 2D methods (Duncan 1996), mitigating potentially conservative estimates of stability from 1D or 2D analyses. An example of an edge effect considered in 3D methods is the lateral shear resistance generated by lateral earth pressure acting against the slope failure's boundary (Arellano and Stark 2000). In order to better characterize the differences between traditional infinite slope analyses and the potential effects of boundary forces on shallow landslide susceptibility, three-dimensional stability methods that represent single or multiple, discrete sliding blocks have been developed (Bellugi et al. 2015; Dietrich et al. 2007a, b; Milledge et al. 2014). These methods demonstrate potential to better characterize landslide susceptibility in realistic terrain that does not broadly meet the aforementioned assumptions implicit in the infinite slope analysis (Milledge et al. 2014).

Vegetation can enhance slope stability via mechanical reinforcement from roots as well as modification of slope hydrology via moisture extraction. Researchers have investigated the mechanical stabilization of roots by modeling root-fiber soil interaction, conducting laboratory tests, and performing in situ tests of root-permeated soils (Gray and Sotir 1996). The limit equilibrium theory developed by Waldron (1977) and Wu et al. (1979) focuses on the tensile strength of root fibers that penetrate the shear zone where sliding occurs and the associated ratio of root area to soil area that occurs at the shear zone interface. By accounting for the angle of shear distortion, the tensile strength is resolved into shear strength components through a Mohr-Coulomb failure relationship. Initially, tensile root strength was incorporated into the infinite slope analysis by increasing the shear resistance along the planar surface at the base of a soil block. However, researchers have shown that the depth of root penetration remains shallow (<2 m) and the reinforcement from lateral roots plays a greater role in stabilizing landslides (Roering et al. 2003; Sakals and Sidle 2004; Schmidt et al. 2001; Schwarz et al. 2010). Despite the many studies that have measured the influence of roots on soil stability, spatial variability of vegetation type and density as well as the associated root structure over a landscape remain a challenge for DEM-based landslide susceptibility mapping (Schmidt et al. 2001). Root reinforcement, which enhances static slope stability, may also provide stabilizing behavior under potentially destabilizing seismic loads (Liang et al. 2015). Seismic influences have also been applied to slope stability analyses as a driving component of failure. Pseudo-static analyses are often utilized for evaluating seismic slope stability, consisting of applying inertial body forces—horizontal and/or vertical—to the failure mass of soil.

Herein, we present a deterministic, shallow landslide susceptibility framework based on a 3D limit-equilibrium model applied to single DEM cells, implemented using statistically derived input parameters from existing landslide inventories. The analysis integrates boundary forces developed from surrounding topography, seismic pseudo-static coefficients that change in magnitude and direction when applying an earthquake motion, soil depth and friction angle calculated from a GIS database of regional shallow landslides, and a convergence analysis to determine appropriate pixel dimensions based on observed landslide dimensions and

analysis of DEMs of varying resolution. To demonstrate implementation of the model, we apply it to a landslide-prone region in the coastal mountains of Oregon, USA. This research (1) presents an approach towards three-dimensional, deterministic shallow landslide susceptibility based on statistical inputs from a given landslide inventory; (2) investigates the effects of discrete boundary forces in context of topography and seismicity; (3) evaluates the reinforcing effects of roots in context of seismicity (both pseudo-static and from scaled earthquake motions); and (4) assesses the impacts of seismicity on infrastructure.

Methodology

Derivation of the three-dimensional topographic limit equilibrium model

The raster-based model developed herein for determining shallow landsliding potential, referred to as the three-dimensional topographic limit equilibrium (3DTLE) model, can be represented by the free-body diagram shown in Fig. 1. The 3DTLE model formulation employs many common assumptions associated with the infinite slope analysis: The failure body is a rigid block of homogeneous soil, landsliding occurs along a planar slip surface, and seepage is oriented in the slope-parallel direction, and the analysis evaluates stability for individual DEM cells. However, in contrast to the infinite slope approach, the slope parallel direction for each given failure body was determined from an aspect raster (azimuthal direction in degrees) derived from a DEM. This consideration of aspect enables the proposed model to account for failure in directions other than X or Y as well as lateral boundary forces. This novel aspect of the work will be discussed in more detail in the following description of methodology. For the given analysis, slope rasters at varying resolutions were generated using the ArcGIS slope algorithm, which calculates the maximum rate of change in a 3×3 cell window (Burrough and McDonell 1998).

Geometric properties of the soil block (Fig. 1) include the width, X ; the slope-parallel length, L ; the height, H ; the slope angle, β (in degrees); and the water height ratio, m . Body forces include the soil weight, W_s , and the horizontal and vertical pseudo-static seismic forces, F_h and F_v . Boundary forces include the weight of trees, W_b ; the normal force, N ; the basal and side shearing forces, S_b and S_s ; the root tensile force, T_u ; and the lateral earth pressure forces, P_{side} , P_{up} , and P_{down} —acting with an inclination angle of δ (in degrees) on the side, upslope, and downslope surfaces, respectively.

Summing forces parallel to the basal slip surface results in

$$S_b + 2S_s + T_u + (P_{down} - P_{up})\cos(\delta - \beta) + (F_v - W_s - W_t)\sin\beta - F_h\cos\beta = 0 \quad (1)$$

and summing forces perpendicular to the basal plane yields

$$N + F_h\sin\beta + (F_v - W_s - W_t)\cos\beta + (P_{down} - P_{up})\sin(\delta - \beta) = 0 \quad (2)$$

For maintaining static equilibrium, it is assumed that the lateral earth pressure forces on the side surfaces, P_{side} , are equal in magnitude and opposite in direction; therefore, there is no movement in the x -direction. The resultant shear and tensile forces in

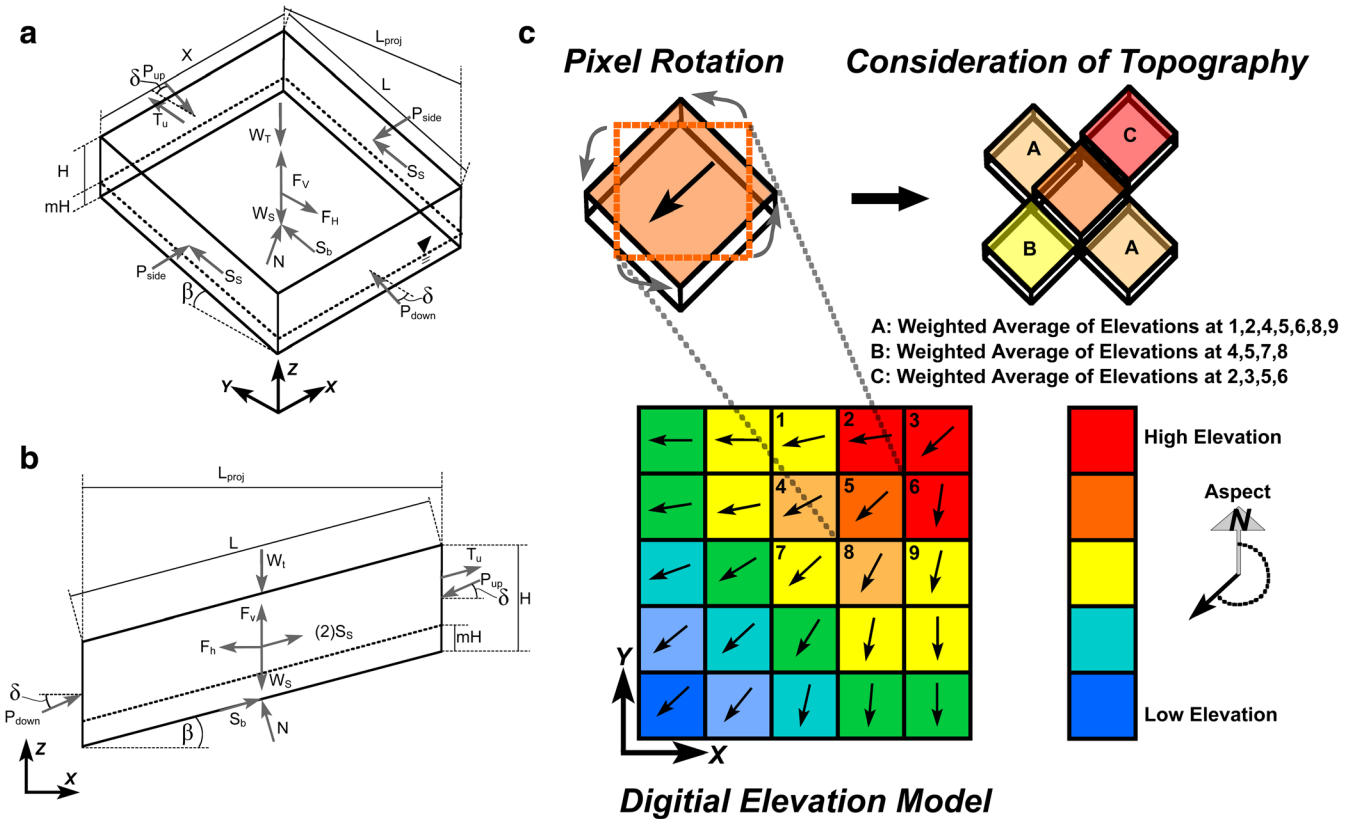


Fig. 1 a Isometric and b profile views of the proposed soil block with associated dimensions and forces. c Example of topographic considerations in analysis

Eq. (1) are expressed as stresses multiplied by the respective area over which they are applied; i.e.,

$$S_b = \tau_b XL \quad (3)$$

$$S_s = \tau_s HL \cos \beta \quad (4)$$

$$T_u = \sigma_u HX \quad (5)$$

where τ_b and τ_s are the shear stresses on the base and side, respectively, and σ_u is the tensile stress on the upslope surface. The shear stress on the failure plane is expressed as shear strength divided by a factor of safety, common practice for most limit equilibrium analyses (Duncan 1996). The effective shear strength, S , of soil is applied to using the Mohr-Coulomb failure criteria

$$S = c' + \sigma' \tan \phi' \quad (6)$$

where c' is the effective soil cohesion intercept, and ϕ' is the effective soil friction angle.

In contrast to a traditional Mohr-Coulomb failure criterion, the present model considers the strength of a combined soil-root system following the theory proposed by Wu et al. (1979). The theory states that the tension in a root fiber can be resolved into components parallel and perpendicular to the shear zone and that a root's contribution to shear strength is given by

$$S_r = t_r (\cos \theta \tan \phi' + \sin \theta) \quad (7)$$

where t_r is the average root tensile strength per soil unit area and θ is the angle of shear distortion. S_r in Eq. (7) can also be referred to as root cohesion, c_r , which is often used in the analysis of shallow slope stability (Bischetti et al. 2005; Gray and Sotir 1996; Wu et al. 1979). Combining Eqs. (6) and (7) with the safety factor produces the following expressions for the shear stress used in Eqs. (3) and (4),

$$\tau_b = \frac{(c' + t_{rb} \sin \theta) + (\sigma'_b + t_{rb} \cos \theta) \tan \phi'}{F_s} \quad (8)$$

$$\tau_s = \frac{(c' + t_{rs} \sin \theta) + (\sigma'_s + t_{rs} \cos \theta) \tan \phi'}{F_s} \quad (9)$$

where t_{rb} and t_{rs} are the root strength terms corresponding to the base and side [obtained by solving for t_r in Eq. (7)] and σ'_b and σ'_s represent the effective normal stresses on the basal and side surfaces, respectively. Because the upslope surface is not a shearing surface, the root fibers do not experience lateral movement and the roots' reinforcing strength is purely tensile. The tensile strength of the roots is defined by

$$\sigma_u = \frac{t_{rs}}{F_s} \quad (10)$$

The normal stresses, σ'_b and σ'_s , in Eqs. (8) and (9) are given by the following expressions,

$$\sigma'_b = \frac{N}{XL} - u_b \quad (11)$$

$$\sigma'_s = \frac{P_{\text{side}}}{HL\cos\beta} \quad (12)$$

where the normal force, N , is obtained by re-arranging Eq. (2) as,

$$N = (W_s + W_t - F_v)\cos\beta + (P_{\text{up}} - P_{\text{down}})\sin(\delta - \beta) - F_h\sin\beta \quad (13)$$

and the pore water pressure at the base, u_b , for seepage parallel with the slope is

$$u_b = \gamma_w m H \cos^2\beta \quad (14)$$

where γ_w is the unit weight of water.

Next, the body forces, F_h , F_v , and W_s , are defined as

$$F_h = k_h W_s \quad (15)$$

$$F_v = k_v W_s \quad (16)$$

$$W_s = HXL\cos\beta[(1-m)\gamma_s + m\gamma_{\text{sat}}] \quad (17)$$

where k_h and k_v are the pseudo-static seismic coefficients in the horizontal and vertical directions, respectively, and γ_s and γ_{sat} are the soil unit weights for dry and saturated conditions, respectively. The 3DTLE model ignores the effects of partially saturated soil (i.e., matric suction) and assumes that the soil below the phreatic surface is saturated and the soil above is dry.

Finally, by substituting Eqs. (3)–(5) and (8)–(17) into Eq. (1) and re-arranging, the following closed-form solution is obtained for the factor of safety against landsliding,

$$F_s = \frac{A_1 c' + A_2 XLt_{rb} + (2A_2 HL\cos\beta + HX)t_{rs} + (A_3 + A_4)\tan\phi'}{A_5} \quad (18)$$

where A_1 through A_5 are defined as

$$A_1 = XL + 2HL\cos\beta \quad (19)$$

$$A_2 = \cos\theta\tan\phi' + \sin\theta \quad (20)$$

$$A_3 = HXL\cos\beta[(1-m)\gamma_s + m\gamma_{\text{sat}}][(1-k_v)\cos\beta - k_h\sin\beta] + W_t\cos\beta - \gamma_w m HXL\cos^2\beta \quad (21)$$

$$A_4 = 2P_{\text{side}} + (P_{\text{up}} - P_{\text{down}})\sin(\delta - \beta) \quad (22)$$

$$A_5 = HXL\cos\beta[(1-m)\gamma_s + m\gamma_{\text{sat}}][(1-k_v)\sin\beta + k_h\cos\beta] + W_t\sin\beta + (P_{\text{up}} - P_{\text{down}})\cos(\delta - \beta) \quad (23)$$

Additionally, the weight of trees can be approximated by the following equation:

$$W_t = \frac{\pi}{4} D_b^2 H_b \rho_b N_t XL\cos\beta \quad (24)$$

in which D_b , H_b , ρ_b , and N_t are average values for diameter, height, wood density, and number of trees per unit area, respectively. The

estimation of tree weight in Eq. (24) is similar to the estimation proposed in Wu et al. (1979), except that Wu et al. (1979) considered a weight per unit area of root mat instead of a weight per unit area of slope.

Lateral earth pressure

To characterize the lateral boundary forces, it is assumed that the earth pressure force acting on the upslope surface results from an active failure wedge, that the earth pressure force acting on the downslope surface results from a passive failure wedge, and that the earth pressure force at the side surfaces can be approximated by at-rest conditions. Significant movement is necessary to mobilize passive earth pressures (James and Bransby 1970), implying that assuming at-rest conditions for the downslope margin is a reasonable alternative assumption. Earth pressure theory is applied to the vertical surfaces of the soil block following Arellano and Stark (2000) and Milledge et al. (2014).

The earth pressure theory used in 3DTLE remains unique, because it includes active and passive seismic earth pressures as well as earth pressures caused by the influence of adjacent topography. The at-rest earth pressure force acting on the side surfaces, P_{side} , is given by

$$P_{\text{side}} = L\cos\beta \left[K_o \left(\frac{1}{2} \gamma_s H^2 + qH \right) - \frac{1}{2} m^2 H^2 \gamma_w \cos^2\beta \right] \quad (25)$$

where $K_o = 1 - \sin\phi'$ is the at-rest coefficient developed by Jaky (1944) for granular soil, and q is the estimated soil surcharge at the lateral boundary, which is a function of adjacent topography. Surcharge is computed as the difference between the elevation of each pixel, and the elevation of the lateral edge is multiplied by the soil unit weight. The average elevation at each lateral boundary is calculated by (1) assigning each elevation pixel the coordinates of its geometric center, (2) drawing a hypothetical cell rotated about the center of the current pixel so that each side is either parallel or perpendicular to slope aspect, (3) estimating the elevation of each vertex of the rotated cell with bilinear interpolation of the elevations from the four nearest pixel centers, and (4) computing the average elevation along each of the rotated cell's lateral edges by averaging values from the two adjacent vertices (Fig. 1c). Lateral forces at the sides must be equal in magnitude, so an arithmetic mean is taken of the two elevation differences. Equation (25) was developed for horizontal soil; accordingly, soil surcharge can result from concave topography [i.e., when lateral elevations are above a cell's elevation, producing a positive surcharge (Fig. 1c)] or convex topography (i.e., when lateral elevations are below a cell's elevation, producing a negative surcharge). The first and second terms inside the brackets of Eq. (25) represent the force per unit length due to soil and water, respectively, and the term outside the brackets is the length over which the lateral earth pressure force acts.

Shukla (2015) and Shukla (2013) provide a framework for computing pseudo-static active and passive earth pressures for c' - ϕ' soils assuming a planar failure surface. The presented equations also include a soil back-slope above the failure wedge. The soil back-slope is approximated by the slope of the considered pixel—a positive back-slope for the active wedge and a negative back-slope for the passive wedge. Adjacent topography increases active pressures and decreases passive pressures at the upslope and downslope surfaces, respectively, because the slope of each

pixel is calculated based on the surrounding elevations. The seismic earth pressure equations were developed for dry soil, but simple modifications can be made for soil with a phreatic surface. Westergaard (1933), for instance, proposes using an average value for soil unit weight and adding a hydrostatic thrust term to the computed soil thrust. The 3DTLE framework does not consider the dynamic response of pore water or the degradation of soil strength that can take place during strong ground motions, but presents a simplified approach as a preliminary investigation. Although the assumption of a planar failure surface may result in overestimation of passive pressures when the angle of interface friction, δ , is large (Choudhury et al. 2004), it is necessary to facilitate reasonable computing times for large datasets. Fortunately, these effects were also reduced by incorporation of back-slope angles. One future alternative approach could include implementation of a curved or composite failure surface, e.g., a log spiral surface (Milledge et al. 2014).

Evaluating the suitability of raster-based susceptibility analyses and appropriate pixel sizes

Shallow landslides may occur in a variety of shapes or sizes, some of which may require more advanced consideration of failure geometry than can be achieved using a raster-based analysis. Nonetheless, raster-based approaches may be suitable when relevant, inventoried slope failures exhibit geometry with an aspect ratio ($L_{\text{projected}}/W$) that is close to unity, where $L_{\text{projected}}$ is the projected length of the slide (different from L , which is the slope-parallel length of the landslide body). When a raster-based landslide susceptibility approach is appropriate, the results will be sensitive to pixel size (Dietrich et al. 2007a, b), so appropriate pixel dimensions should be assessed based on the dimensions of the observed landslides. In this approach, a raster-based analysis is used to evaluate susceptibility while accounting for varying pixel dimensions, slope, aspect, and boundary forces. There are varying approaches to evaluate the dimensionality of inventoried landslides; in this study, side lengths of the rectangles were determined in ArcGIS using the minimum bounding geometry tool, which fits multiple rectangles to a given polygon and selects the one with the smallest area. Based on the prevailing slope aspect within the bounding box, the rectangular dimensions were characterized as being parallel or transverse to the direction of motion. Using this technique on a given landslide inventory, the statistical distribution of aspect ratio and landslide area can be determined as a probability density function (PDF) and a cumulative distribution function (CDF) to better assess observed landslide shape. With these statistical distributions, a mean aspect ratio near unity demonstrates that employing a raster-based analysis may be suitable for evaluating landslide susceptibility.

Discretization of the DEM and its derivatives is a function of the distribution of inventoried landslide dimensions—evaluation of various resolutions better captures the distribution of potential landslide sizes. Within the 3DTLE model, the failure area is limited to the size of each pixel in the given DEM (Fig. 1). Critical landslide sizes, the discretized pixel dimensions that are best representative of inventoried landslides, are unknown prior to performing the analysis, so it is necessary to evaluate a range of failure sizes through the input of several DEM resolutions. CDFs were developed for a given suite of DEM resolutions to investigate the relationship between pixel size (area of a square pixel),

susceptibility, and observed shallow landslide area. Baseline pixel dimensions were attained from the landslide inventory by calculating the square root of the area of each polygon, providing a distribution of pixel dimensions (Fig. 2). These values deliver a CDF of pixel dimensions that can be compared against distributions of pixel dimensions that fail (i.e., $FS \leq 1$) using the 3DTLE model with a back-analysis of geotechnical properties from the landslide inventory and other inputs (water table, seismic coefficient, root reinforcement). The back-analysis of each landslide is determined by using relevant metadata (slope, observed depth of failure, area), and discretizing the observed surface into a raster form (Fig. 2). The distribution of unstable pixel dimensions are attained by calculating the total failed area for each given resolution normalized to the total failed area for all resolutions, ultimately producing a CDF when these percentages are cumulatively summed. The calculated CDF for resolution can then be compared to the CDF representative of the landslide inventory for assessing suitability. Furthermore, a series of pixel sizes representative of the majority of observed and calculated slope failures (e.g., between 10 and 90% of landslides) can be selected for implementation in evaluating landslide susceptibility. This requires less computational time for evaluating susceptibility over large regions than selecting many increments of pixel dimensions without a priori knowledge of landslide size. A user may elect to simply select pixel dimensions based on a given landslide inventory; however, in this analysis, the authors have used the comparison of pixel dimension CDFs as a means of calibrating assumed input parameters and evaluating the sensitivity of landslide size to the given inputs.

Application of the 3DTLE model

Overview of analyses and associated geospatial data

The flowchart depicted in Fig. 3 provides a simplified illustration of the various steps of the presented framework. Three main input sources—a shallow landslide inventory, DEMs, and earthquake records—enable the primary forms of the 3DTLE analysis presented in this study. To demonstrate the 3DTLE model, a location near Gales Creek, Oregon, was selected, because the density of the lidar-derived landslide inventory was robust. Located approximately 50 km west of Portland, the selected area features a narrow valley flanked by steeper forested slopes. State Highway 8 and Gales Creek run the length of the valley, and several smaller roads lie within the valley and upon the hillslopes. Within this study, the 3DTLE model was used to (a) back-analyze 100 inventoried shallow landslides in a 40-km² DEM (analysis A); (b) evaluate landslide susceptibility and critical landslide size in the same DEM under a variety of groundwater, root, and seismic conditions (analysis B); (c) evaluate landslide susceptibility and effects on infrastructure for a larger 150-km² DEM (analysis C); and (d) assess the landsliding behavior of a 2-km² tile under an actual, scaled seismic motion representative of a subduction zone earthquake (analysis D), all shown in Fig. 4. An overview of analyses, purposes, inputs, and outputs are outlined in Table 1. Seismicity is of particular concern as the Cascadia Subduction Zone lies in close proximity to the study area, meaning that potential fault activity is capable of producing earthquakes with larger magnitudes and earthquake motions with greater durations than shallow crustal earthquakes (Rong et al. 2014).

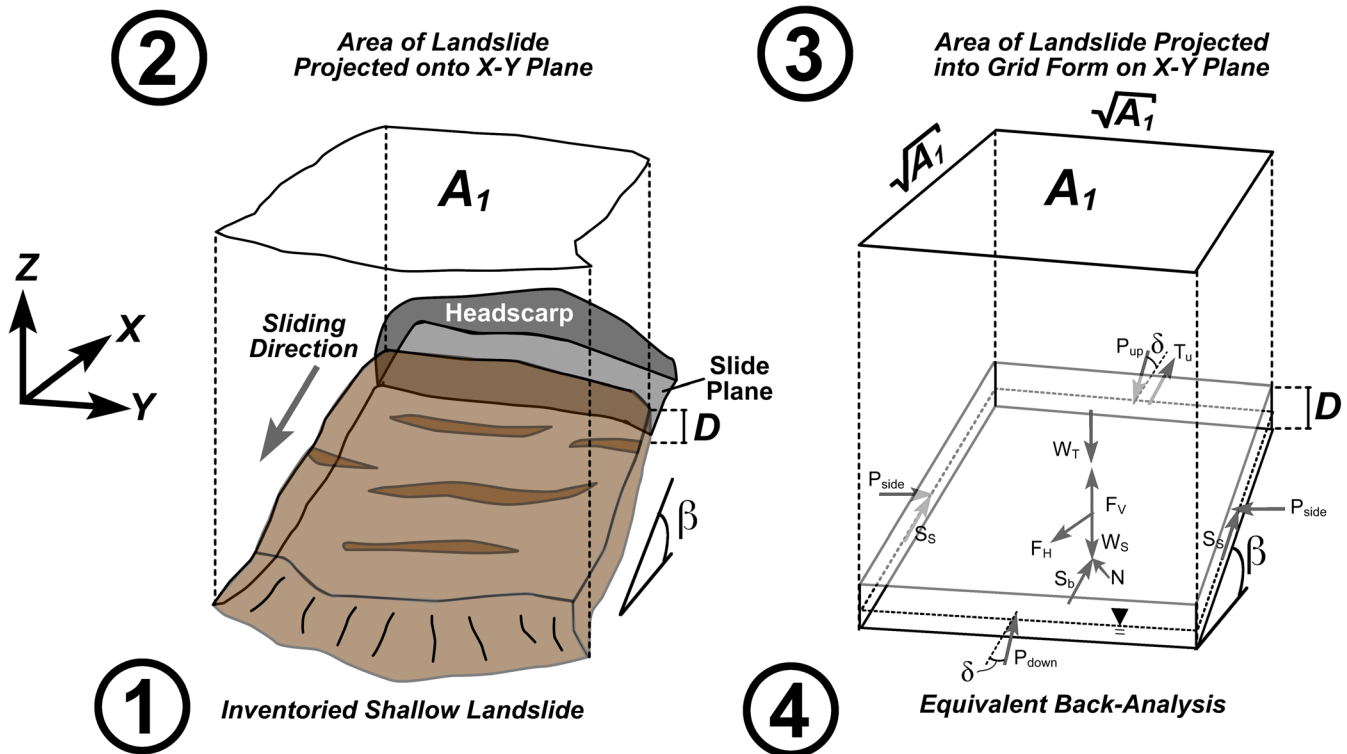


Fig. 2 Projection and conversion of inventoried landslides into 3DTLE analysis

Shallow landsliding is prevalent in the Oregon Coast Range of the USA. There are tens of thousands of landslide deposits mapped as part of the Statewide Landslide Information Database for Oregon (SLIDO), provided by the Oregon Department of Geology and Mineral Industries (DOGAMI). The SLIDO V.3 (Burns et al. 2012) database contains digitized polygons of past landslide deposits with various attributes, such as landslide movement type and depth of failure, that were mapped based on topographic features (e.g. headscarps, deposits). In addition to the landslide deposit inventory, the SLIDO database also contains a larger inventory of landslide points based on observed failures with no shape or depth data associated with them. Landslide polygons are fewer in number as the manual mapping and entry of associated metadata is a slow and painstaking process (Leshchinsky et al. 2015); in the studied 150-km² region, these polygons are only available in the southern reaches and were used for back-analysis. The landslide point inventory is far more extensive, as it is populated by observations from the state transportation department, geologic surveys, and land management agencies and therefore could be used to assess model agreement with the larger region that does not have a full polygon inventory. The point-based inventory lacks associated metadata for landslide shape and size—they do, however, provide information regarding the approximate time of occurrence. DOGAMI manages bare earth lidar DEMs for much of Western Oregon (supported by the Oregon Lidar Consortium), which exclude vegetation, with a resolution of 0.9 m.

Calculation with the 3DTLE model was performed with MATLAB R2015b software, and the ArcGIS 10.2.2 software was used for visualization and manipulation of spatial data. All of the analyses took place on a computer with 128 GB of RAM and

two processors running at 2.6 GHz, using the Windows 7 operating system. Computation time varied for each susceptibility mapping procedure, requiring approximately 1.5 min per analyzed square kilometer.

Soil and root properties

A critical component of evaluating slope stability is the use of appropriate soil shear strength parameters. The 3DTLE model was applied to the landslide inventory to characterize soil strength for the regions of interest. To investigate back-calculation of representative soil strengths, the following assumptions were made: (1) landslide deposit attributes such as failure depth, slope, and area are representative of pre-failure conditions; (2) the polygon area representing shallow landslide deposits can be approximated as a square shape for a given body of rupture (Fig. 2); (3) selected landslide records failed under static conditions (i.e., k_h and k_v are zero); and (4) the soil is unconsolidated and mobilized drained soil strength conditions at failure (i.e., only ϕ' was used, $c' = 0$). Then, the soil strength was back-calculated by assuming a factor of safety of unity for a set of landslide dimensions. Soil unit weights for dry and saturated conditions are assumed to be 15 and 16 kN/m³, respectively, based on values published in Wu and Sidle (1995) for a study site near Mapleton, Oregon. The assumptions are an idealized representation of regional soil conditions, but present a means of using the regional slope stability model to attain meaningful data for susceptibility mapping; that is, a user may select appropriate soil conditions based on site investigations or back-calculated failures. Future modifications of this susceptibility framework could benefit from information regarding causative factors and timing

Table 1 Overview of analyses, objectives, inputs and outputs

Analysis	Area	Objective	Inputs	Outputs
A	40 km ²	Back-analysis of object-based landslide inventory for statistical distributions of geotechnical input properties and landslide pixel dimensions	<ul style="list-style-type: none"> • DEM • Slope • Aspect • m • k_{fh} • c_r • Pixel size • Landslide inventory 	<ul style="list-style-type: none"> • Statistical distribution of shear strength for susceptibility analyses • Statistical distribution of landslide depth for susceptibility analyses • Selected pixel sizes for susceptibility analyses • Baseline water height ratio
B	40 km ²	Application of 3DTLE towards smaller map to observe sensitivity of greater array of input parameters	<ul style="list-style-type: none"> • DEM • Slope • Aspect • m • k_{fh} • c_r • Pixel size 	<ul style="list-style-type: none"> • Susceptibility analysis in consideration of water height ratio, c_r, and k_{fh}
C	150 km ²	Application of 3DTLE towards a larger map to evaluate correspondence of landslide susceptibility model with infrastructure	<ul style="list-style-type: none"> • DEM • Slope • Aspect • m • k_{fh} • c_r • Pixel size • Oregon Highway Geodatabase 	<ul style="list-style-type: none"> • Susceptibility analysis for larger region and infrastructure in consideration of c_r and k_{fh} • Comparison towards point-based landslide inventory
D	2 km ²	Application of 3DTLE to observe time-dependent failure under a given earthquake acceleration-time history	<ul style="list-style-type: none"> DEM Slope Aspect m k_{fh} c_r Pixel size 	<ul style="list-style-type: none"> • Cumulative failed area with respect to time- and aspect-dependent earthquake acceleration

For this framework, back-calculation of soil strength using the landslide inventory required tree properties and root reinforcement. Root cohesion can vary depending on tree species, age, environment, and spatial scale. Sakals and Sidle (2004) applied a spatially variable model to determine root cohesion in the Oregon Coast Range, which was determined as 4.4 kPa for natural forest. Roering et al. (2003) back-calculated a root cohesion of 11 kPa from a back-analyzed landslide in the Oregon Coast Range. The current study uses a root cohesion value of 8 kPa, an approximate mean of the values reported by Sakals and Sidle (2004) and Roering et al. (2003). Best estimates of tree properties for the Oregon Coast Range are defined as $D_t = 0.75$ m, $\rho_t = 6$ kN/m³, $H_t = 40$ m, $N_t = 400$ stems/ha, $d_r = 1$ m, and $\theta = 60^\circ$, as described in previous studies (Roering et al. 2003; Sakals and Sidle 2004; Wu et al. 1979). Note that the typical depth of root penetration is 1 m (Sakals and Sidle 2004); therefore, root cohesion is only calculated over a 1-m depth and then averaged over the full depth of the soil block. For example, when c_r is 8 kPa over a meter of root penetration depth and the shear zone is 2 m in depth (i.e., 1 m below the root penetration depth), the averaged c_r is 4 kPa. The vertical surcharge of tree weight per unit area is calculated as 4.4 kPa, similar to the 5.2 kPa value reported by Wu et al. (1979). This average tree surcharge, presented in Eq. (24), was assumed to correspond to trees with average root cohesion of 8 kPa (c_{r-avg}). In order to adjust the tree surcharge (based on tree height/age) with respect to input root cohesion parameters, the tree surcharge was scaled by a factor of c_r/c_{r-avg} in parametric studies. This relationship may be complex, but is considered

linear in this framework to simplistically observe the effects of varying forest density or age.

Since the time and conditions of each unique slope failure is unknown, one may choose conditions observed in recent, well-documented landslides; however, selection of the modeling input values can have significant implications on soil strength and subsequent susceptibility mapping. The approach used herein provides a framework for selecting an array of soil strength properties and shear plane depths based on past landslides, enabling statistically derived inputs that may enhance the evaluation of landslide susceptibility within a specific region. Accordingly, the sensitivity of back-calculated soil strength was determined for 100 representative shallow landslides by varying input parameters—including water height ratio and root cohesion (analysis A). The sensitivity analysis produced a suite of mean friction angle values (Fig. 5) as a function of water height ratio and root cohesion. The soil surcharge term was neglected during calculation of the lateral earth pressures because a pre-slide DEM was not available. Mean back-calculated friction angles generally span a large range of values depending on the input parameters and the given landslide inventory; accordingly, it is difficult to specify a single value of friction angle for evaluating regional landslide susceptibility. For demonstrative purposes, the baseline conditions for the shallow landslide inventory were considered to be 8 kPa of root cohesion (forested conditions at failure) and a water height ratio of 0.5 (observed for shallow landslide failures in coastal Oregon; Roering et al. 2003), corresponding to a mean friction angle of 32.5°, used only in the evaluation of landslide size and time-dependent seismicity analysis.

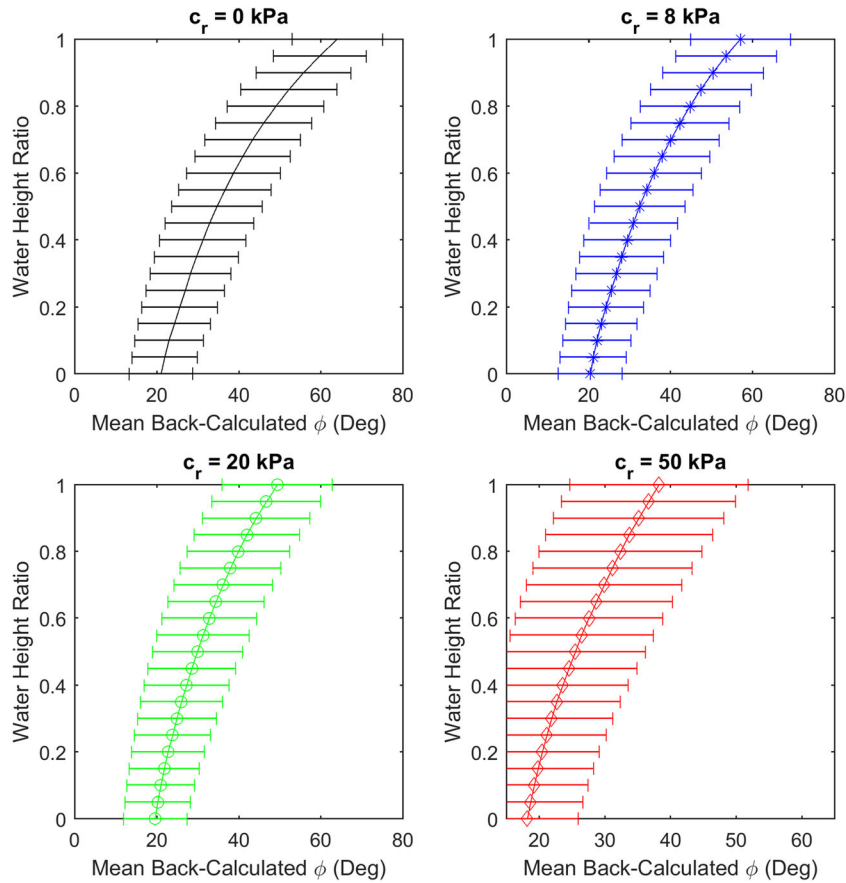


Fig. 5 Mean back-calculated friction angle for changing values of water height ratio and root cohesion

However, for susceptibility analyses, the back-analyzed shear strength properties are derived from a given landslide inventory by means of a probability density function of ϕ , representative of the statistical distribution of shear strength attained from each individual landslide in the given inventory (Fig. 6). The soil shear strength is dependent on other properties that are statistically derived from prior literature, including root cohesion, water height ratio, and soil unit weight. Root cohesion is defined as a fixed value that was determined statistically in previous studies (e.g., Wu et al. 1979; Roering et al. 2003; Sakals and Sidle 2004). The water height ratio, m , has a major influence on the determination of back-calculated friction angles, and varying root cohesion also affects the back-calculated friction angles, especially when m is large. Herein, $m = 0.5$ was chosen as the water height ratio for the baseline case (analyses A and D). A half-saturated soil depth ($m = 0.5$) is thought to be reasonable, as it has been observed that shallow landslides in Coastal Oregon often occur when the water table is less than half the depth of failure (Roering et al. 2003). The location of a water table varies throughout a landscape in reality (Fan et al. 2007); however, in this study, it was selected as an input parameter for sensitivity analyses and model calibration. Soil unit weight can vary depending on lithology, geology, site conditions, and saturation levels°in this study, statistically derived relationships describing bulk unit weights of forest soils in Oregon were used (Wu and Sidle 1995). Future modifications to the framework could better assess the spatial

variability of water table depth and its effects on shallow landsliding with field-verified observations using traditional piezometers or other remote sensing tools (e.g., soil moisture active passive (SMAP) satellite data). Furthermore, incorporation of not only water table depth but also the effects of unsaturated soil behavior

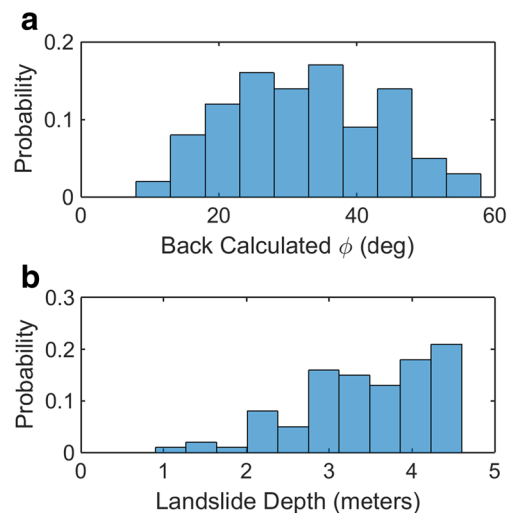


Fig. 6 Probability distributions of **a** back-calculated friction angles for baseline conditions and **b** landslide depths obtained from the shallow landslide inventory

may enable improved back-analysis and assessment of shallow landsliding susceptibility (Godt et al. 2009).

Analysis of landslide size and shape for study area

As described in the methodology, landslide sizes and shapes in the SLIDO inventory were investigated to (1) evaluate the suitability of a raster-based approach and (2) determine pixel sizes that are sufficiently representative of observed landslide dimensions. Slide dimensions and shapes were evaluated by bounding each inventoried polygon with a rectangle and considering the dominant aspect of the bounding box (Fig. 7a). A PDF and a CDF of the inventoried landslide aspect ratio, shown in Fig. 7b, demonstrate a mean length to width ($L_{\text{projected}}/W$) ratio of 1.36 and a peak probability for a ratio of approximately 1.0, demonstrating that use of a raster-based approach is reasonable. However, it should be noted that implicit consideration of (1) an active, driving wedge at the top of the landslide body, (2) a passive resisting wedge at the toe of the landslide body, and (3) the actual length of a given landslide body being greater than its square projection due to slope demonstrates aspect ratios that are greater than unity, similar to observations made in prior literature (e.g., Milledge et al. 2014, where aspect ratios for several inventories was primarily between 1 and 2). Future work could incorporate algorithms that better capture the arbitrary shape of landslides by clustering pixels to better capture actual landslide morphology (Bellugi et al. 2015).

Since appropriate raster discretization is unknown prior to running the 3DTLE model, a range of DEM resolutions were evaluated to investigate the relationship between pixel size and failure probability. A suite of ten DEMs ranging from 3 to 140 m in resolution were bilinearly re-sampled from the 0.9-m source DEM using baseline mean back-calculated soil shear strength ($\phi = 32.5^\circ$) and mean depth of observed failure (3.6 m) as inputs and compared to the dimensions of landslides in the corresponding inventory (Fig. 8). Sensitivity of input parameters on relevant pixel dimensions was assessed for a range of input root cohesions, water height ratios, and horizontal seismic coefficients which were also

applied to demonstrate the effect on the calculated failure area, highlighting larger effective landslide areas for higher water heights and seismic coefficients (Fig. 8). The baseline scenario and inventory are represented in all three plots while considered input values range from 0 to 50 kPa for root cohesion, 0 to 1 for water height ratio, and 0 to 0.3 for horizontal seismic coefficient. The curvature of the CDFs depicted in each of the three plots provides a relative measure of which pixel sizes are causing the most failure; steeper curves translate to a majority of failures caused by a small range of cell sizes, while a curve with a more shallow gradient signifies that many cell sizes contributed to the calculated area of failure. Root cohesion had minimal effect on the distribution of failure among pixel sizes as evidenced by the similar trend of the closely spaced CDFs (Fig. 6a). While the increase of root strength decreased landslide susceptibility, it did so relatively evenly amid the ten considered DEM resolutions. Figure 7b shows the variation of the water height ratio, which greatly affects the size of predicted failure. For $m = 0$, approximately 90% of the failures took place for pixel sizes less than 30 m with a mean pixel dimension of 10 m, while full saturation ($m = 1$) demonstrated failure that was distributed across significantly larger pixel sizes (mean of 35 m). The addition of seismicity (Fig. 6c) revealed an increase in landslide size; increasing k_h from 0 to 0.3 increased failure among larger pixel sizes, representative of a mean landslide dimension changing from 25 to 32 m. Of the presented CDFs, the case when $m = 0.5$ was selected as it follows the observed landslide CDF reasonably, while accounting for smaller landslides that may not have captured in the manually mapped landslide inventory (e.g., when $m = 0.75$). The CDF for $k_h = 0.1$ also demonstrates reasonable agreement, but there is little information in the presented inventory to affirm that the observed shallow landslides were caused by seismic activity; therefore, the baseline conditions were considered to be $m = 0.5$, $c_r = 8$ kPa, and $k_h = 0$. For the baseline case, approximately 90% of the failures occur from pixel dimensions less than or equal to 60 m. To expedite computational time of susceptibility analyses for large regions, four DEM resolutions representative of even increments between

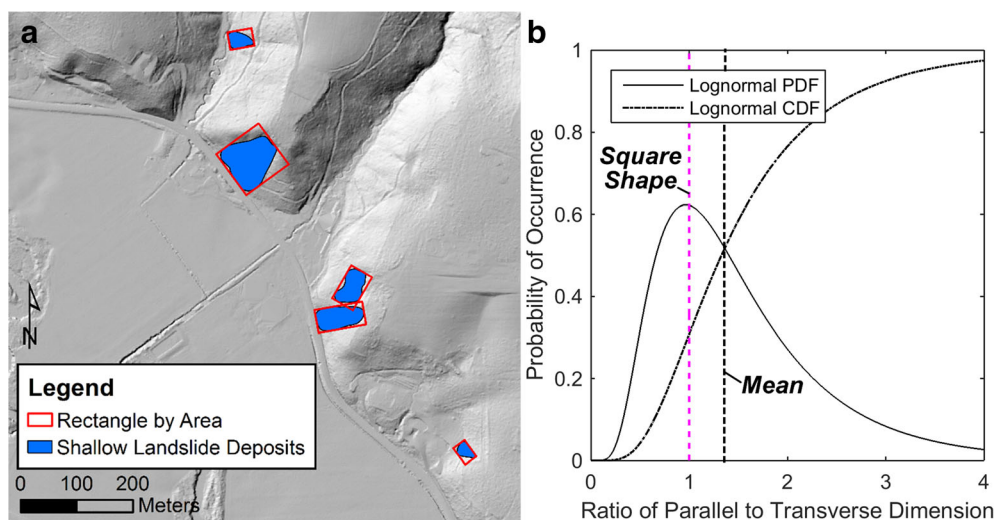


Fig. 7 Analysis of landslide shape. **a** An example of fitting rectangles to landslide deposit polygons. **b** The ratio of rectangular dimensions are depicted as probabilities of landslide occurrence

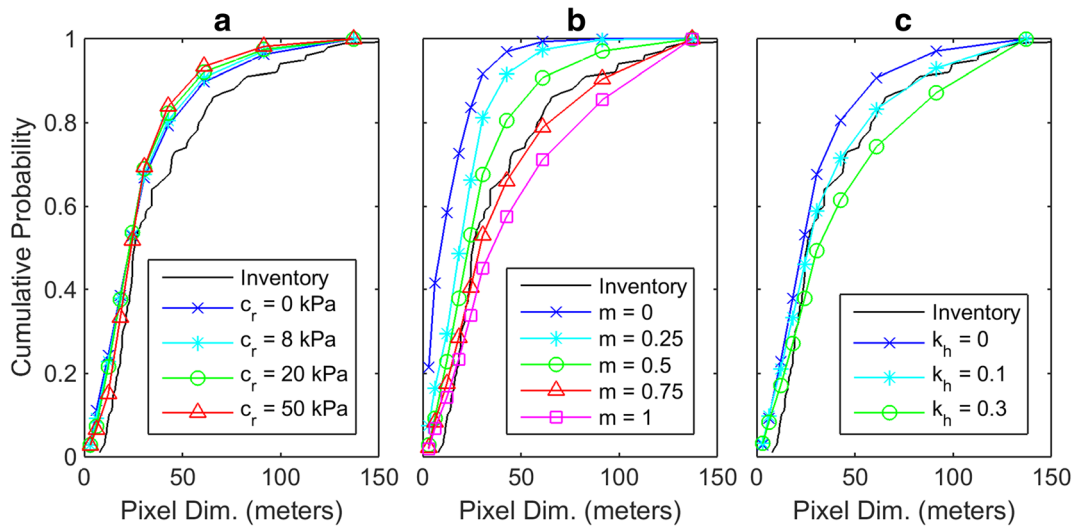


Fig. 8 The dependence of failure on pixel size for changing values of **a** root cohesion, **b** water height ratio, and **c** horizontal seismic coefficient. Baseline conditions used for non-changing parameters

10th and 90th percentiles of landslide failures were selected: 6, 18, 30, and 61 m.

A reliable shallow landslide inventory is required for assessing landslide susceptibility. The 3DTLE method assumes that inventoried landslide deposits can be modeled with a square shape (Fig. 2), which affects the back-calculated soil strength. Recall that the mean ratio of landslide dimensions was roughly 1.36 (Fig. 5). Because the inventoried polygons represent landslide deposits and not the pre-failure soil mass, it is likely that the pre-failure soil mass maintained an aspect ratio (length/width) closer to unity, and failure caused an increase in the dimension parallel to movement. After failure, the landslide body displaced downslope, implying that the mapped landslide dimensions, including both the headscarp and body, may be slightly longer than the pre-failure dimensions. While the shallow landslide deposit polygons vary in shape, the data presented in Fig. 7 and the implicit use of active and passive wedges at the upper and lower boundaries of a slide support the assumption of a square shape for the purpose of applying the raster-based 3DTLE model.

Although landslide inventories are useful for performing regional slope stability analyses, they can introduce uncertainty into analyses. Primarily, landslide records are based on observations from published maps; therefore, many smaller slope failures were likely not noticed or detectable, which indicates that the distribution of landslide area is skewed towards larger sizes. The bias towards larger landslides implies that the shallow landslide inventory CDF presented in Fig. 8 is also shifted to the right, corresponding to larger pixel sizes. The bias towards larger landslide areas further supports the selection of $m = 0.5$ and $c_r = 8$ kPa as the baseline scenario because the baseline scenario CDF is positioned to the left of the landslide inventory CDF in each plot. If the smaller landslide areas were included in the landslide inventory, then the inventory CDFs would likely shift near the baseline CDFs in Fig. 8; accordingly, the baseline case could be regarded as more accurate representation of landslides in the Gales Creek area.

Susceptibility analysis

In this analysis, landslide susceptibility was founded on the shallow landslide inventory obtained from SLIDO. Instead of using “baseline” soil conditions ($\phi = 32.5^\circ$, depth = 3.6 m), back-calculated soil friction angle and depths of failure from individual landslides were treated as variables having probability distributions determined from the forensic analysis of the inventory for $m = 0.5$ and $c_r = 8$ kPa (analysis B, Fig. 6). The respective product of a given friction angle and potential depth of failure (both corresponding to a specific probability) were used as input for a given slope stability analysis. Due to the inherent reliance on back-calculated strength and landslide depth for input, this susceptibility analysis is heavily dependent on the quality of the landslide inventory.

To apply susceptibility mapping, distributions of landslide depth and back-calculated friction angle were divided into ten bins, with each bin having a mean value and an associated probability of failure (Fig. 8). The analysis was run 100 times for each combination of friction angle and depth for four different DEM resolutions. The selected resolutions—6, 18, 30, and 61 m—were considered representative of the baseline CDF curve, as will be highlighted in the “Results and discussion” section. Varying pixel sizes were integrated into a singular susceptibility map by overlaying the calculated areas of failure with a resolution equal to the smallest cell dimension. If failure ($F_s < 1$) was calculated for a given cell, then the cell was assigned the product of the two probabilities, friction angle and depth. Finally, the probabilities were summed for a given cell, producing a map where each cell has a probability of failure between 0 and 100%.

The susceptibility analysis was first applied to a 40-km² tile that contained the landslide inventory for quality control and then projected to a much larger, 150-km² DEM of the watershed, delineated using the ArcGIS Hydrology toolset (analysis C, Fig. 4). Infrastructure susceptibility was characterized for major roads within the large DEM as a means of evaluating the impacts of shallow landsliding on regional infrastructure lifelines. All major roads were included in the analysis. This susceptibility was

represented as the maximum probability of failure occurring within 15 m of the roadway's centerline under the conditions of each susceptibility map to account for failures that develop under the roadways or in close proximity. Note that it does not account for slope failures further than 15 m that may have significant runout distances.

Seismic analysis

A seismic analysis that accounted for an actual scaled earthquake motion was performed to highlight the capability of the 3DTLE model (analysis D). To reduce computational expense, only one earthquake motion was selected rather than perform a robust seismic analysis considering many possible motions of the locale. The most significant earthquake hazard at Gales Creek results from the Cascadia Subduction Zone, which is capable of producing large magnitude earthquakes (up to M9.0) and long-duration earthquake motions. The earthquake motion used herein was selected from recordings of the 2011 Great East Japan Earthquake, because the earthquake motions produced by the Cascadia Subduction Zone are expected to have similar amplitudes, frequency contents, and durations (Goldfinger et al. 2012; Melgar et al. 2016). The selection was made by fitting a database of the 2011 Great East Japan Earthquake motions, which was compiled and processed by Carey (2014) based on recordings from K-net and KiK-net seismic stations, to a target design spectrum. The target design spectrum was created for Gales Creek using the ASCE 7-10 (2010) procedure with a site class D assumption. The earthquake motions were linearly scaled in the time-domain and fitted to the target design spectrum using a root mean square error (RMSE) goodness-of-fit algorithm (Barbosa et al. 2014; Kottke and Rathje 2008). The earthquake motion with the best RMSE goodness of fit and the lowest linear scaling factor was chosen. The acceleration-time series for the East-West and North-South transverse components of the selected earthquake motion, as well as the earthquake response spectra and target design spectrum, are shown in Fig. 9.

Within a limit equilibrium slope stability framework, these complex earthquake motions can be simplified as pseudo-static forces; i.e., the inertial force caused by the earthquake motion shaking the slope mass is estimated as a static force (Seed and Martin 1966). The horizontal pseudo-static seismic coefficient, k_h , is estimated from the amplitude of a target acceleration time-series so that each acceleration value (in g) corresponds to a dimensionless k_h that was applied to the 3DTLE model. Notably, most researchers apply a reduction factor to the acceleration value to obtain the value of k_h for engineering design, which varies from approximately 0.5 (e.g., Hynes-Griffin and Franklin 1984) to 0.75 (e.g., Bray and Rathje 1998). However, given that the seismic analysis performed herein is a proof of concept, and that most k_h reduction factors are calibrated for earthen dams and other embankment structures, a "reduction factor" of 1.0 is assumed for analysis (i.e., the acceleration values are equivalent to the k_h values). At a given time increment, the 3DTLE model used a horizontal pseudo-static seismic coefficient for a given cell. The EW and NS k_h values were rotated to the direction of the given pixel's aspect using direction cosines, which created cell-specific k_h values. In this manner, each cell of a DEM has a unique horizontal pseudo-static seismic coefficient that was used for the factor of safety calculation. For the seismic analysis, a mean depth (3.6 m) and a mean back-calculated strength ($\phi = 32.5^\circ$) were used, as opposed to the probability distributions used for the susceptibility analysis, to expedite computational time.

Similar to the susceptibility analysis, four DEM resolutions were used to calculate regions of failure and overlaid onto one map. This process was repeated for each time step of the earthquake motion to produce an animation of the cumulative failed area. An analysis of the full 300-s motion produces 30,000 frames, resulting in considerable computing expense. Accordingly, a reduced motion and a smaller DEM tile (blue rectangle in Fig. 4) were used for the seismic analysis.

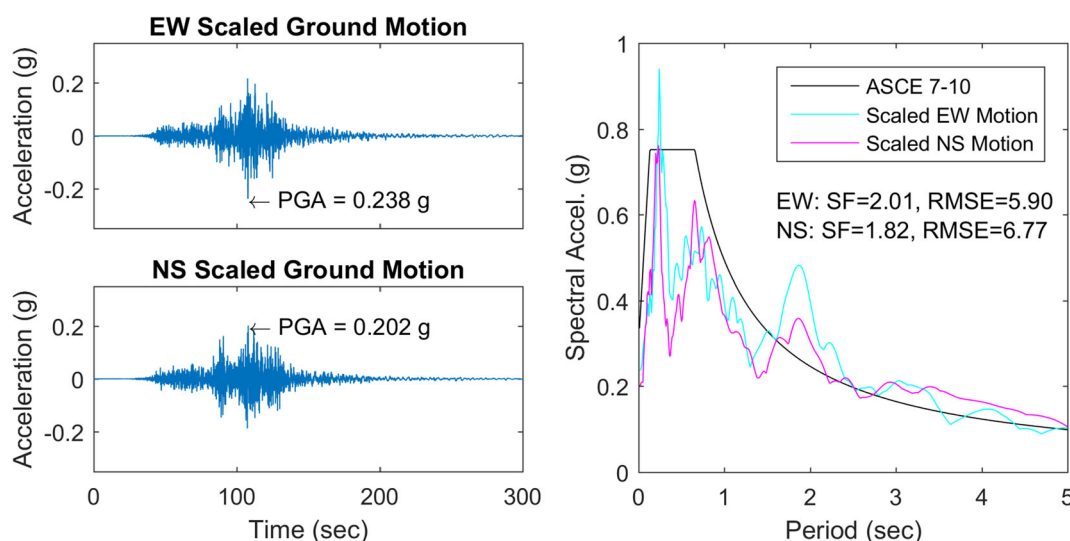


Fig. 9 EW and NS acceleration-time series for the full-length scaled ground motions (left) and pseudo-spectral response with the design target spectrum (right) of two selected motions used in the scaling of 46 input motions

Comparison to observed landslides

Results from the 3DTLE model were compared to historical landslide data points (SLIDO) in the larger study region to determine the model's suitability for predicting future slope instability (Fig. 10). These landslide data points generally lack complete information about landslide shape or depth, unlike the inventory of polygons used in back-calculation of strength, but provides a simple means of assessing model agreement within the larger DEM. In the studied region, data points were primarily recorded from 1996, a year of historic rainfall. A sensitivity analysis was performed on water height ratio under the assumption that the majority of the observed landslides were rainfall-induced (n.b., no significant earthquake motions were recorded in Oregon during 1996; the largest nearby earthquake had a magnitude of 5.4 and occurred near Duvall, Washington, nearly 350 km from Gales Creek). The 3DTLE model was used to predict the probability of landsliding at each of the points identified as a landslide in the SLIDO database for the Gales Creek watershed in 1996. Thus, comparing the 3DTLE model-calculated probability of failure with locations of known failure provides an approximate measure of validation for using the 3DTLE model to assess shallow landslide susceptibility (Fig. 10).

Susceptibility maps of the greater Gales Creek region were generated for four values of water height ratio, and focal statistics were applied to smooth the results in a 3 × 3 cell window. Focal statistics were applied to mitigate some of the positional uncertainty effects of comparing discrete point objects (SLIDO points) with an underlying raster. The susceptibility was queried at 84 landslide points, and histograms were produced of the results (Fig. 10). The input water height ratios used were $m = 0, 0.25, 0.5, \text{ and } 0.75$, and the horizontal seismic coefficient as well as root cohesion remained zero. In addition, similar histograms were

generated for 84 random points in locations where landslides had not occurred to show a reverse correlation. The histograms are depicted on the left plot of Fig. 10 with a map of point locations on the right plot. The 3DTLE model should predict high probabilities of failure at the known landslide points from the SLIDO database, which would suggest model validation, to a rough approximation. The 3DTLE model does predict high probabilities of failure when $m = 0.5$ and $m = 0.75$, where the model shows that 70 and 85% of the known SLIDO landslide points have probabilities of failure greater than 0.4, respectively. In contrast, the 3DTLE model performed at the random points should predict the opposite trend; that is, a majority of random points should have low probabilities of failure, which indicates that the model is not an over-predicting failure at locations other than at the landslide points. The 3DTLE model does predict low probabilities of failure when $m = 0$ and $m = 0.25$ (42 and 50% of SLIDO points have failure probabilities greater than 40%, respectively). Notably, the histogram for $m = 0.5$ shows a roughly inverse distribution of probabilities of failure across the bin sizes, which gives further credence for using $m = 0.5$ as the baseline case. Although the sensitivity analysis performed to compare the model performance to observed data is relatively simplistic, it shows that the 3DTLE model can reasonably capture slope failures that have been observed, and it shows that the 3DTLE model is appropriately sensitive to the location of the phreatic surface.

Susceptibility analysis

Four DEM resolutions (6, 18, 30, and 60 m) and distributions of both landslide depth (1.1 to 4.4 m, Fig. 7) and friction angle (10.5° to 55.5° for $m = 0.5$, Fig. 6) were applied to produce susceptibility maps for different variations of horizontal seismic coefficient, water height ratio, and root cohesion (analysis B). Considered input values included $k_h = 0, 0.1, 0.3, 0.6$; $m = 0, 0.25, 0.5, 0.75$; and $c_r = 0, 8, 20$ kPa. When applied to the 40-km² DEM containing

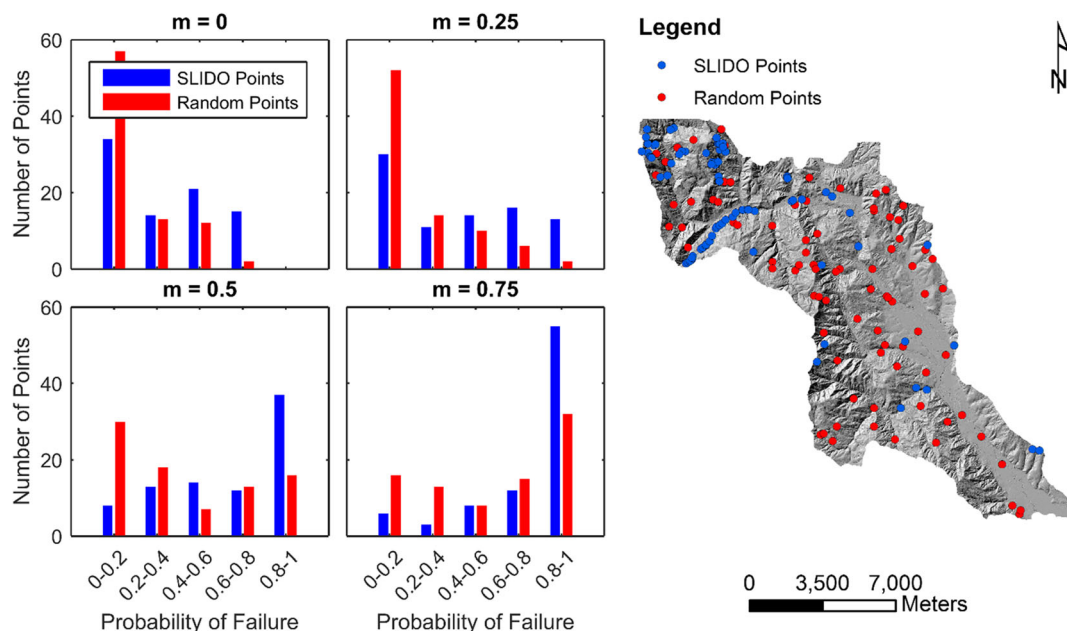


Fig. 10 Histograms of calculated susceptibility at observed landslide points and randomly generated points for four different values of input water height ratio. The map of the Gales Creek watershed (right) features 84 points from the SLIDO database and 84 randomly generated points in locales without landslides

the landslide inventory, susceptibility maps were produced (Fig. 11), where map colors range from dark blue (0% probability of failure) to dark red (100% probability of failure). The increased height of water and seismicity caused an increase in the probability of failure for the sloped terrain along the edges of the valley (Fig. 11). To quantify the effect of changing input values, the mean probability of failure is compared for the 48 different combinations of k_h , m , and c_r (Fig. 12). The mean probability of failure for these scenarios is directly proportional to the water height ratio and the horizontal seismic coefficient, but inversely proportional to root cohesion. As is expected, increasing horizontal seismic coefficients increased the mean probability of failure. For example, when m was 0.25 and c_r was 0 kPa, the mean probability of failure increased from 0.12 to 0.82 when k_h transitioned from 0 to 0.6, respectively. Increasing the root cohesion to 20 kPa reduced the probability of failure to 0.65 when k_h was 0.6. When the water table was high ($m = 0.75$), increasing root cohesion from 0 to 20 kPa reduced the mean probability of failure by between 10 and 12%; however, this behavior was muted when seismic inputs were great ($k_h = 0.6$) as the large seismic forces overcame the stabilizing forces of the roots.

Using the soil strength and depth distributions of the shallow landslide inventory, corollaries were made about the statistical probability of slope failure occurring, resulting in susceptibility maps for various root, water, and seismic scenarios. The 48 different scenarios featured in Fig. 12 were investigated as a parametric study with highly variable input parameters (i.e., the input parameters can change temporally and spatially with environmental factors or be difficult to estimate as “mean” values on a landscape scale). However, scenarios with $m = 1$ were excluded from the susceptibility analysis, because water tables are rarely, if ever, at the ground surface in mountainous terrain, and excluding $m = 1$

cases reduced computational expense. Furthermore, root cohesion has a larger effect on landslide susceptibility for shallower slides, primarily when the landslide depth is less than the depth of root penetration and basal root reinforcement can be applied to the 3DTLE model. The generated susceptibility maps, such as those of Fig. 11, provide important information about shallow landslide susceptibility, namely, the spatial extent and magnitude of failure probabilities. Regions with high probabilities of failure can be identified over large extents, yet the accuracy of a given map is dependent on the accuracy of several parameters (e.g., friction angle, root cohesion, soil depth, water height ratio) to characterize the considered landscape.

The results of susceptibility mapping at an extended spatial scale (analysis C, Figs. 13 and 14) highlight the notable impacts that seismicity may have in mountainous terrain with metastable slopes. Four cases of horizontal seismic coefficient, water height ratio, and root cohesion were considered in the calculation of failure probabilities, each showing increasing probability of failure with greater seismic accelerations. Omission of root cohesion demonstrated a small increase in landslide susceptibility, but was minimal in comparison to seismicity. This increasing susceptibility of failure under seismicity translates directly to greater susceptibility for infrastructure (Fig. 12). Roads that were influenced most were located on or adjacent to steep hillsides that were deemed likely to fail. As horizontal seismic coefficients increased, roads that were in proximity to gentler slopes realized greater susceptibility from landslides.

Finally, the maps of Figs. 13 and 14 include a significantly larger area (150 km²) than the rectangular maps of Fig. 11, which indicates that the susceptibility analysis relies on an inventory that is only partially representative of the landscape. Nonetheless, this analysis still demonstrates that landslide susceptibility can be characterized

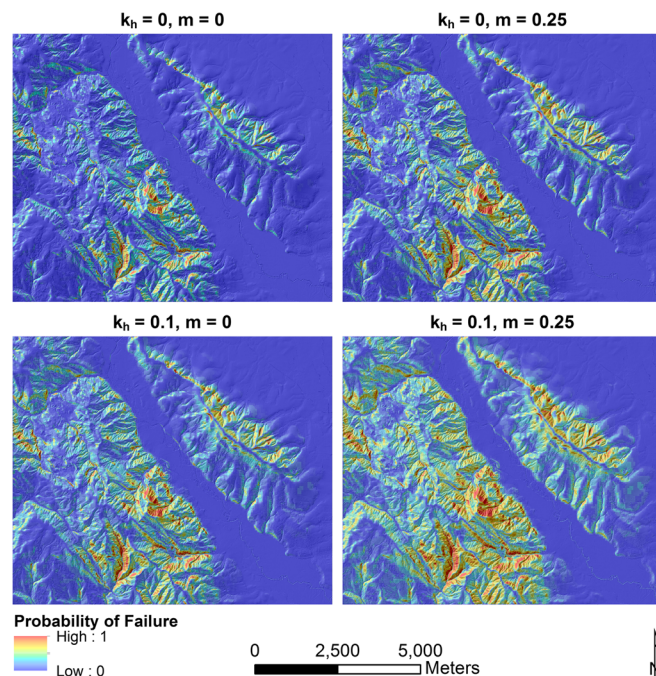


Fig. 11 Landslide susceptibility maps of Gales Creek, OR, calculated using a product distribution and various input values of horizontal seismic coefficient and water height ratio. Root cohesion was held constant at 0 kPa for all four maps

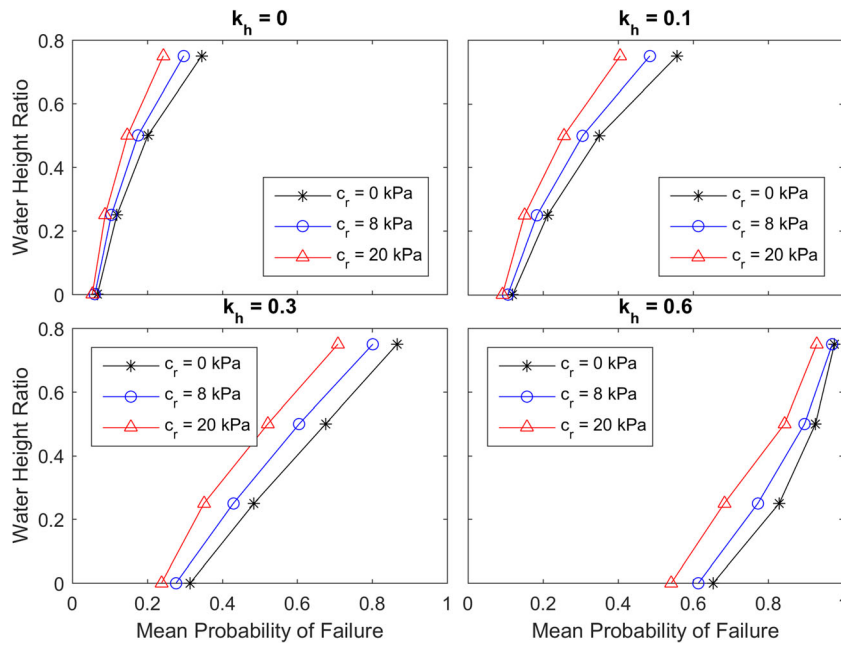


Fig. 12 Comparison of the mean probability of failure calculated for various input values of horizontal seismic coefficient, water height ratio, and root cohesion

for large extents based on given distributions of soil properties determined from back-analysis of existing landslides. To improve the larger regional landslide susceptibility maps, accurate representation between the considered inventory deposits and the mapping extents should be maintained, which is usually accomplished by considering mapping extents with similar conditions as the inventory (e.g., lithology, soil type, hydrologic conditions). The main advantage of extending a mapped area is that meaningful conclusions can be made in areas where shallow landsliding may not yet have occurred. For instance, the infrastructure susceptibility maps of Fig. 14 can aid in asset management decisions and emergency repair. Although the infrastructure susceptibility maps display similar probabilities of failure as their associated landslide susceptibility maps, they capture the potential for infrastructure loss associated with nearby shallow landslides.

Seismic analysis

The factor of safety against slope stability for each cell was calculated for every time step of the aspect-rotated earthquake motion, which ensured that local and global peak accelerations were considered in the analysis (analysis D). Accordingly, the k_h values at each time step were applied to the shallow landslide model, producing a temporal map of the cumulative failed area. Final calculated areas of failure for maps produced by the four combinations of m and c_r , listed in Fig. 15, are approximately 222,740 m² (7.10% of map area), 196,840 m² (6.28%), 337,500 m² (10.8%), and 326,610 m² (10.4%), respectively. From this analysis, it can be surmised that root strength plays a nuanced role in preventing seismically induced shallow landslides that is more pronounced when lower water tables are considered.

Note that there are some discontinuities in the cumulative area of failure time series (Fig. 15), which correlate to “spikes” in the acceleration-time series. The spikes in the acceleration-time series can be investigated further by examining the Husid plot, which

shows the normalized Arias intensity (Arias 1970) buildup versus time. Arias intensity, I_A , is given as

$$I_A = \frac{\pi}{2g} \int_0^{t_d} \dot{u}(t)^2 dt \quad (26)$$

where $a(t)$ is the acceleration-time series and t_d is the duration of the earthquake motion. Accordingly, significant changes in the slope of the Husid plots correspond to the spikes in the acceleration-time series, and $d(I_A)/dt$, which is sometimes referred to as the shaking intensity rate (Dashti et al. 2010), is shown in the bottom plot. The first major discontinuity in the cumulative area of failure time series occurs around 55 s and corresponds to the first series of larger $d(I_A)/dt$ values (primarily from the N-S earthquake motion). The second major discontinuity in the cumulative area of failure time series occurs around 75 s and corresponds to the largest $d(I_A)/dt$ values (primarily from the E-W earthquake motion). Although the earthquake motion continues to produce large values of $d(I_A)/dt$ after 75 s, no more significant changes to the cumulative area of failure occur.

Comparison to conventional infinite slope analyses

Conventional analyses of shallow landslide susceptibility have often been applied using the infinite slope analysis, which prompts a comparison between the conventional analyses and the 3DTLE analyses to highlight notable differences, particularly potential conservatism associated with the infinite slope method. The comparison focused on landslide susceptibility for four combinations of horizontal seismic coefficients and water height ratios, using the binned distributions of friction angle and landslide depth (Fig. 16) in the 40-km² DEM. The infinite slope equation developed by Hadj-Hamou and Kavazanjian (1985) was used for calculations, which accounts for slope parallel seismic accelerations; accordingly, the magnitude of the input horizontal seismic acceleration was

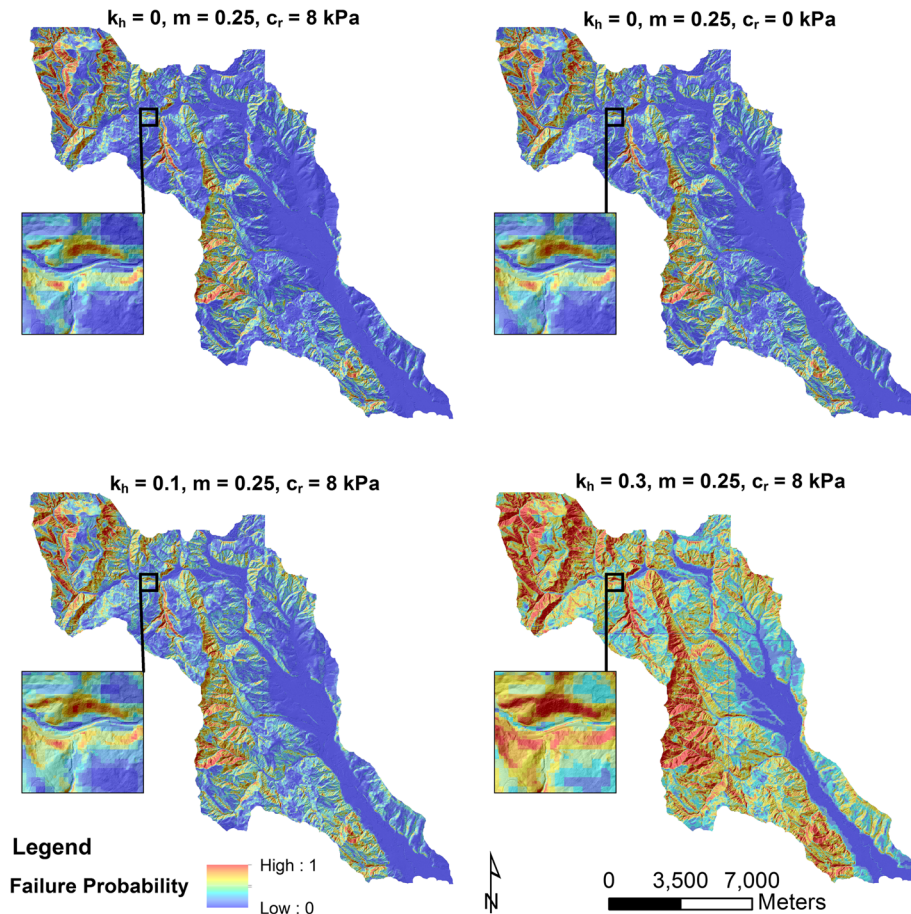


Fig. 13 Susceptibility map for the Gales Creek watershed showing the probability of failure for four cases of horizontal seismic coefficient, water height ratio, and root cohesion overlaid on *shaded relief*. The *inset map* shows a close-up view of a section of Highway 6

projected to a slope parallel direction to maintain consistency between the conventional and 3DTLE analyses. Root cohesion and tree weights were neglected from this analysis for simplicity in comparisons.

A raster subtraction was employed to observe the spatial impact of the infinite slope analysis's assumptions versus the 3DTLE model, which includes boundary forces (Fig. 16). Two-dimensional slope stability methods, like the infinite slope analysis, predict lower factors of safety against slope failure than three-dimensional methods—meaning that the infinite slope method should, on average, predict higher probabilities of failure than the 3DTLE model. Subtracting the 3DTLE failure probability from the infinite slope failure probability produced a map of probability differences; a positive difference signifies that the infinite slope analysis calculates a higher probability of failure, whereas a negative difference denotes higher failure probabilities calculated with the 3DTLE model. For static cases, the infinite slope analyses predict higher susceptibility to landsliding in an average sense (Fig. 16), both with and without the presence of water, although the analysis with $m = 0.25$ under static conditions does begin to indicate small regions where the 3DTLE model predicts higher landslide susceptibility. As the factors driving failure are increased (water height ratio and seismic coefficient), the 3DTLE model produces more regions with higher failure probabilities on the

shallower sections of the landscape (i.e., ridges). The 3DTLE model is more sensitive to seismic forces, because the seismic forces act both as body forces in the potential landslide body and as driving forces in both the neighboring active and passive wedges. Although the suitability of the infinite slope method is a function of topography and underlying soil strata, this comparison does indicate notable conservatism for discrete shallow landslides, particularly under lower water height ratios and seismicity.

Constraints, limitations, and opportunities for future work

This study proposes the 3DLTE, a raster-based methodology, for using landslide inventories to derive statistical geotechnical and landslide properties to assess landslide susceptibility deterministically; however, as in any landslide susceptibility modeling, there is significant uncertainty in input parameters, particularly those relating to the subsurface. The aforementioned susceptibility analyses use root cohesion as a uniform value applied over a landscape, despite the fact that vegetation can range significantly regionally. Future work could better delineate root reinforcing behavior by accounting for root properties associated with unique tree species, age, and site conditions. Groundwater table in these analyses was input as constant over a landscape for each analysis; however, in reality, varying groundwater tables would be observed, depending on geographic location, geology, lithology, and

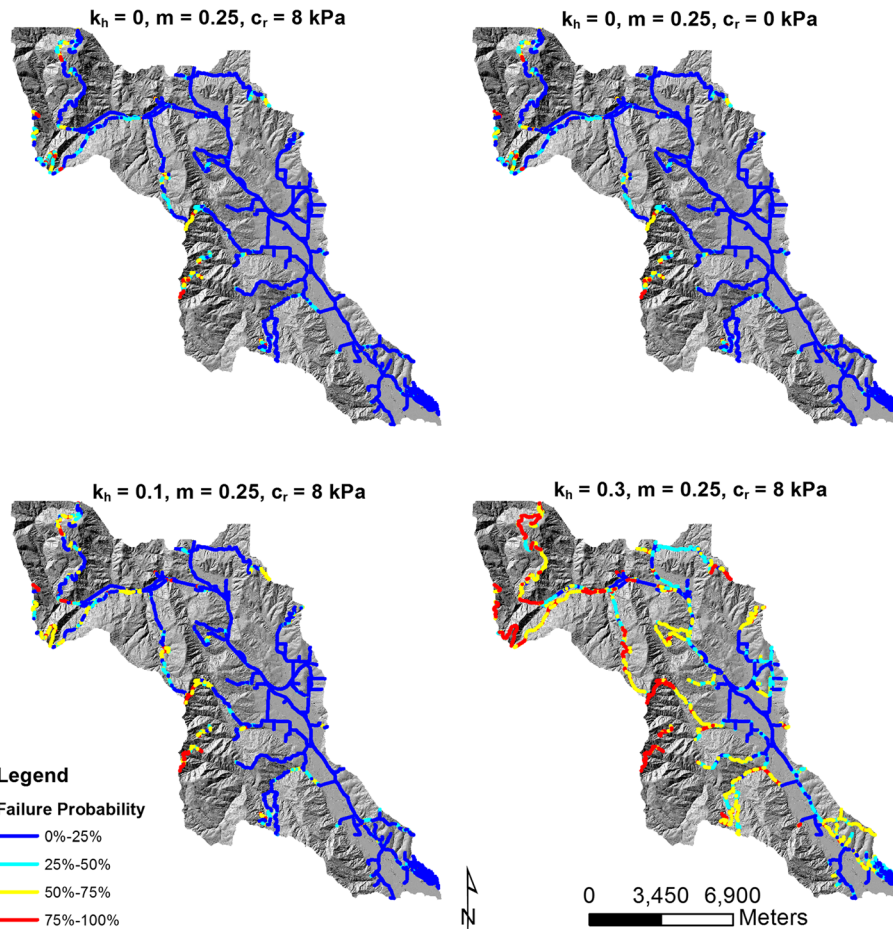


Fig. 14 Infrastructure susceptibility maps for various cases of horizontal seismic coefficient, water height ratio, and root cohesion overlaid on *shaded relief maps* within the Gales Creek watershed

topography. Future work could use remote sensing data or a field instrumentation network to better define the hydrologic conditions and associated variability on a regional level. The proposed methodology uses a landslide inventory to better define statistical regional properties pertaining to landslide susceptibility. However, this means that the quality of derived input properties is intrinsically dependent on the quality of a given landslide inventory and its associated metadata. This is particularly important when considering the uncertainty surrounding the causative conditions for a given landslide. In the polygon-based inventories used in this study, there is no information about landslide causation (e.g., past earthquakes, rainstorms, wildfire) or time of occurrence. Therefore, assumptions surrounding initial conditions at the time of failure were made and sensitivity analyses performed. Future work could benefit from large landslide inventories with enhanced detail regarding causative factors of landsliding—this would enable better forensics and, consequently, better input properties for susceptibility. The proposed framework uses a raster-based analysis to calculate susceptibility at various meaningful pixel sizes while also considering the slope aspect for a given landslide mass; however, future modifications of the proposed methodology could use improved algorithms to account for the often complex kinematics and geometry of realistic landslides. For example, recent

work has used clustering algorithms to account for the stability of multiple pixels representative of arbitrary landslide geometry. Such analyses, although computationally expensive at large scales, would more robustly capture potential landslide geometry. Furthermore, future analyses could adopt more complex failure kinematics, including rotational (e.g., log-spiral) or generalized slope stability kinematics (e.g., Spencer, Morgenstern-Price)—however, the use of such methods introduces further levels of uncertainty regarding three-dimensional conditions in the subsurface. Despite these possibilities for enhancements, in its current form, the presented framework presents a rational methodology for using landslide inventories and a newly developed raster-based, three-dimensional slope stability model to account for regional conditions, topography, and potential seismic loading when evaluating shallow landslide susceptibility.

Conclusions

A framework for assessing shallow landslide susceptibility—through the development of the three-dimensional topographic limit equilibrium (3DTLE) model, a shallow landslide inventory, lidar-derived digital elevation maps (DEMs), and various geotechnical scenarios—was developed. This 3DTLE model is unique because it accounts for lateral root reinforcement along multiple surfaces, characterizes the influence

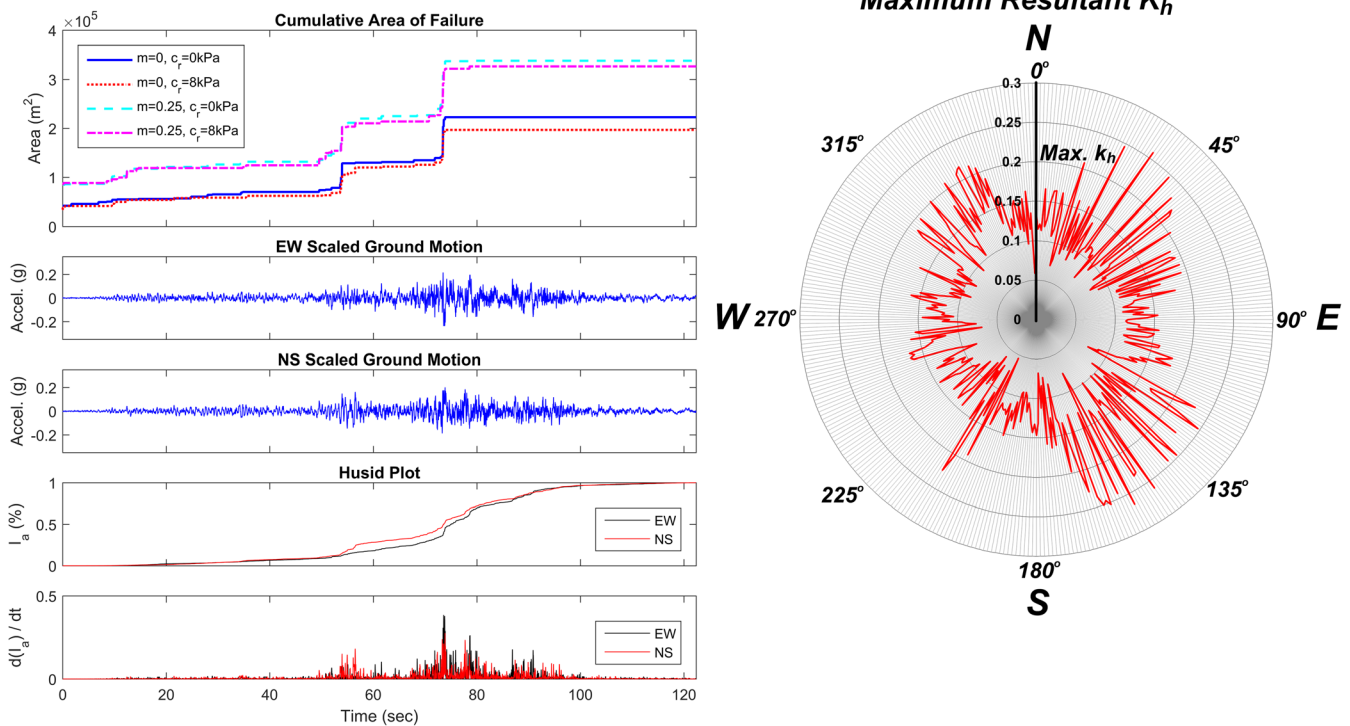


Fig. 15 Cumulative area of failure obtained by applying the shorter length motions to a smaller DEM tile near Gales Creek, OR. Four different combinations of water height ratio and root cohesion were analyzed

of adjacent topography through the earth pressure boundary forces, accounts for temporally and directionally variant pseudo-static seismic forces, and uses deterministic geotechnical slope stability analyses and applies them to a regional scale.

Based on the 3DTLE modeling, it was shown that shallow landslide susceptibility may be sufficiently modeled using a raster-based structure to approximate landslide shape for certain landslide inventories. This observation is particularly valid when accounting for implicit boundary wedges (active and passive) and basing the landslide shape on post-rupture landslide remains, which are often delineated as one shape despite possible runout and dilation during failure. Furthermore, the results of the 3DTLE modeling indicate that landslide susceptibility can be determined for the landscape scale when reasonable input parameters (e.g., those from existing landslide inventories) are used. The integrated approach of using existing landslide inventories to determine probability distributions of landslide depth, landslide size, and back-calculated soil shear strengths provides an alternative deterministic approach to landslide susceptibility mapping under both static and seismic conditions.

Earthquake motions (i.e., seismically induced ground displacement, velocity, and acceleration) are directionally dependent; for instance, the earthquake motion in a north-south transverse direction is different than the earthquake motion in an east-west transverse direction. Prior research has demonstrated a correlation between the directionality of ground motions and the aspect of co-seismic landslides (Barlow et al. 2015). The presented framework could be an investigatory tool to further evaluate this relationship by taking an acceleration-time history and comparing its

directionality with modeled shallow landslide occurrence. Within this study, that seismically induced landsliding depends on the “intensity” of the earthquake motion oriented in the downhill slope direction, defined as a vectorized pseudo-static coefficient during a given time step. Therefore, the occurrence seismically induced landsliding is very sensitive to the selected input earthquake motion, which must be estimated for a given location. However, this model presents a unique framework towards evaluating non-uniform and time-dependent accelerations.

A comparison of the 3DTLE model to conventional infinite slope analysis shows that three-dimensional slope stability tools can better capture the effects of topographic features, including valleys and ridges. Additionally, conventional infinite slope analysis may be unconservative when seismic loading of discrete landslides is considered, as it cannot capture the effects of increased driving forces (upslope active wedge) and decreased resisting forces (downslope passive wedge) during inertial loading.

There are many potential opportunities to refine the 3DTLE model. Root reinforcement can be analyzed in a way that captures the variation in root area ratio from alternative data sets (e.g., NVDI). A more accurate characterization of passive pressure can be obtained by considering a curved failure surface. Strength parameters can be better categorized by incorporating observed regional geologic units. Incorporation of unsaturated soil mechanics and hydrologic modeling may help capture the effects of partial saturation and infiltration, yielding better understanding of rainfall-induced landslides. Topographic amplification can be integrated to evaluate the effects of non-uniform seismic accelerations on slope stability (e.g., Ashford et al. 1997). Finally, the approach can be

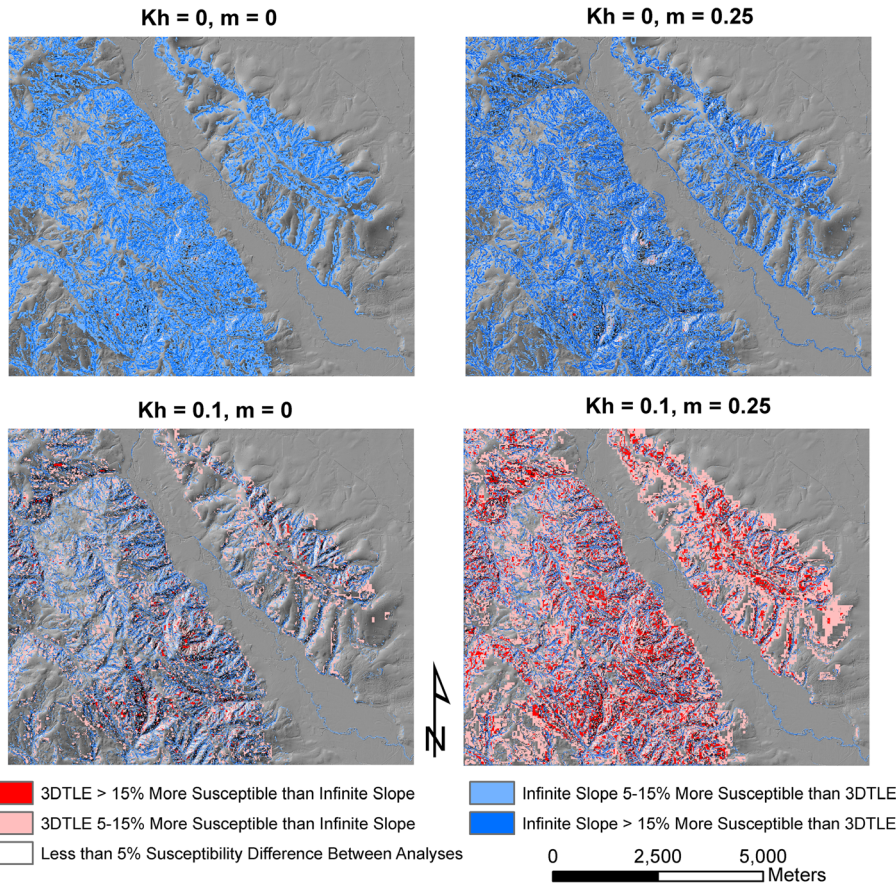


Fig. 16 Difference in failure probability between the infinite slope analysis and the 3DTLE model for several cases. A positive difference signifies that the infinite slope analysis calculated a higher probability of failure, while a negative difference means 3DTLE calculated a higher probability

further translated into infrastructure risk maps by considering proximity and vulnerability of infrastructure such as roads, business districts, or residential areas. The future directions are evidently formidable; however, improved landslide modeling will ultimately help decision makers in regions prone to landsliding.

A_{1-5} , coefficients used in factor of safety; c'' , effective soil cohesion; c_r , root cohesion; D_t , tree diameter; d_r , depth of root penetration; F_h, F_v , horizontal and vertical seismic forces; F_s , factor of safety; H , height of soil block; H_t , tree height; K_o , coefficient of at-rest earth pressure; k_h, k_v , horizontal and vertical pseudo-static seismic coefficients; L , slope-parallel length of soil block; L_{proj} , pixel length of soil block; m , water height ratio; N , normal force; N_t , number of trees per unit area; P_{down} , lateral earth pressure force at downslope surface; P_{side} , lateral earth pressure force at side surface; P_{up} , lateral earth pressure force at upslope surface; q , soil surcharge at side surface; S_b, S_s , shearing force at base and side; S_r , root cohesion; T_u , tensile force at upslope surface; t_{rb}, t_{rs} , average root tensile strength per soil unit area; u_b , porewater pressure at base; W_s , soil weight; W_t , tree weight; X , width of soil block; β , slope angle; γ_d, γ_{sat} , dry and saturated soil unit weight; γ_w , unit weight of water; δ , interface friction angle; θ , angle of shear distortion; ρ_b , density of wood; σ''_b, σ''_s , normal stress at base and side surfaces; σ''_u , tensile stress at upslope surface; τ_b, τ_s , soil shear stress at the base and side surfaces; ϕ'' , effective soil friction angle.

Acknowledgements

The authors appreciate the lidar data provided for this study by the Oregon Lidar Consortium and DOGAMI. They would also acknowledge partial funding for this project by the Oregon Department of Transportation (SPR 786). Additional support by the National Institute of Food and Agriculture, U.S. Department of Agriculture, McIntire Stennis project under 1002779 is acknowledged.

References

- Arellano D and Stark TD (2000) "Importance of three-dimensional slope stability analyses in practice." Geotechnical Special Publication, 18–32
- Arias A (1970) Measure of earthquake intensity. Massachusetts Inst. of Tech., Cambridge. Univ. of Chile, Santiago de Chile
- ASCE (2010) Minimum design loads for buildings and other structures. Standards, American Society of Civil Engineers
- Ashford SA, Sitar N, Lysmer J, Deng N (1997) Topographic effects on the seismic response of steep slopes. Bull Seismol Soc Am 87(3):701–709
- Ayalew L, Yamagishi H (2005) The application of GIS-based logistic regression for landslide susceptibility mapping in the Kakuda-Yahiko Mountains, Central Japan. Geomorphology 65(1):15–31
- Barbosa AR, Mason HB, Romney K et al. (2014) "SSI-Bridge: soil-bridge interaction during long-duration earthquake motions." University of Washington, Seattle, WA, USDOT University Transportation Center for Federal Region, 10
- Barlow J, Barisin I, Rosser N, Petley D, Densmore A, Wright T (2015) Seismically-induced mass movements and volumetric fluxes resulting from the 2010 M w= 7.2 earthquake in the Sierra Cucapah, Mexico. Geomorphology 230:138–145

- Bellugi D, Milledge DG, Dietrich WE, McKean JA, Perron JT, Sudderth EB, Kazian B (2015) A spectral clustering search algorithm for predicting shallow landslide size and location. *Journal of Geophysical Research: Earth Surface* 120(2):300–324
- Bischetti GB, Chiaradia EA, Simonato T, Speziali B, Vitali B, Vullo P, Zocco A (2005) Root strength and root area ratio of forest species in Lombardy (Northern Italy). *Plant Soil* 278(1–2):11–22
- Bray J, Rathje E (1998) Earthquake-induced displacements of solid-waste landfills. *J Geotech Geoenviron Eng* 242–253. doi: 10.1061/(ASCE)1090-0241(1998)124:3(242)
- Burns WJ, Madin IP, Ma L (2008) “Statewide Landslide Information Database for Oregon (SLIDO), Release 1.” 2008 Joint Meeting of The Geological Society of America, Soil Science Society of America, American Society of Agronomy, Crop Science Society of America, Gulf Coast Association of Geological Societies with the Gulf Coast Section of SEPM
- Burns WJ, Duplantis S, Mickelson KA et al. (2012) “Landslide inventory maps of the Gales Creek quadrangle, Washington County. 3rd ed.” Portland: Oregon Department of Geology and Mineral Industries
- Burrough PA, McDonell RA (1998) Principles of geographical information systems. Oxford University Press, New York, p 190
- Carey TJ (2014) “Multi-hazard framework and analysis of soil-bridge systems : long duration earthquake and tsunami loading.” M.S. thesis, School of Civil and Construction Engineering, Oregon State University, Corvallis, Oregon
- Carrara A, Cardinali M, Detti R, Guzzetti F, Pasqui V, Reichenbach P (1991) GIS techniques and statistical models in evaluating landslide hazard. *Earth Surf Process Landf* 16(5):427–445
- Choudhury D, Sitharam TG, Rao SK (2004) “Seismic design of earth-retaining structures and foundations.” *Current science*, 87(10)
- Dai FC, Lee CF (2002) Landslide characteristics and slope instability modeling using GIS, Lantau Island, Hong Kong. *Geomorphology* 42(3):213–228
- Dashti S, Bray J, Pestana J et al. (2010) Centrifuge testing to evaluate and mitigate liquefaction-induced building settlement mechanisms. *J Geotech Geoenviron Eng* 918–929. doi: 10.1061/(ASCE)GT.1943-5606.0000306
- Dietrich WE, Reiss R, Hsu M-L, Montgomery DR (1995) A process-based model for colluvial soil depth and shallow landsliding using digital elevation data. *Hydrol Process* 9(3):383–400
- Dietrich WE, McKean J, Bellugi D, Perron T et al. (2007a) “The prediction of shallow landslide location and size using a multidimensional landslide analysis in a digital terrain model.” Proceedings of the fourth international conference on debrisflow hazards mitigation: Mechanics, prediction, and assessment (DFHM-4). Chengdu, China 10–13
- Dietrich WE, McKean J, Bellugi D et al. (2007b) The prediction of shallow landslide location and size using a multidimensional landslide analysis in a digital terrain model
- Duncan JM (1996) State of the art: limit equilibrium and finite-element analysis of slopes. *J Geotech Eng* 122(7):577–596
- Fan Y, Miguez-Macho G, Weaver CP et al. (2007) Incorporating water table dynamics in climate modeling: 1. Water table observations and equilibrium water table simulations. *Journal of Geophysical Research: Atmospheres*, 112(D10)
- Godt JW, Baum RL, Lu N (2009) Landsliding in partially saturated materials. *Geophys Res Lett* 36(2)
- Goldfinger C, Nelson CH, Morey AE, et al. (2012) Turbidite event history—methods and implications for Holocene paleoseismicity of the Cascadia subduction zone: U.S. Geological Survey Professional Paper 1661–F, 170 p
- Gray DH and Sotir RB (1996) Biotechnical and soil bioengineering slope stabilization: a practical guide for erosion control. Wiley
- Hadj-Hamou T, Kavazanjian E Jr (1985) Seismic stability of gentle infinite slopes. *J Geotech Eng* 111(6):681–697
- Hervás J and Bobrowsky P (2009) “Mapping: inventories, susceptibility, hazard and risk.” *Landslides—disaster risk reduction*, K. Sassa and P. Canuti, eds., Springer Berlin Heidelberg, 321–349
- Hopkinson C, Chasmer L, Barr AG, Kljun N, Black TA, McCaughey JH (2016) Monitoring boreal forest biomass and carbon storage change by integrating airborne laser scanning, biometry and eddy covariance data. *Remote Sens Environ* 181:82–95
- Hynes-Griffin, ME, Franklin AG (1984) Rationalizing the seismic coefficient method (No. WES/MP/GL-84-13). Army Engineer Waterways Experiment Station Vicksburg Ms Geotechnical Lab
- Iida T (2004) Theoretical research on the relationship between return period of rainfall and shallow landslides. *Hydrol Process* 18(4):739–756
- Jaboyedoff M, Oppikofer T, Abellán A, Derron MH, Loye A, Metzger R & Pedrazzini A (2012) Use of LIDAR in landslide investigations: a review. *Nat Hazards* 61(1):5–28
- Jaky J (1944) The coefficient of earth pressure at rest. *Journal of the Society of Hungarian Architects and Engineers* 78(22):355–358
- James RG, Bransby P (1970) Experimental and theoretical investigations of a passive earth pressure problem. *Geotechnique* 20(1):17–37
- Jibson RW, Harp EL, Michael JA (2000) A method for producing digital probabilistic seismic landslide hazard maps. *Eng Geol* 58(3):271–289
- Kottke A, Rathje EM (2008) A semi-automated procedure for selecting and scaling recorded earthquake motions for dynamic analysis. *Earthquake Spectra* 24(4):911–932
- Leshchinsky BA, Olsen MJ, Tanyu BF (2015) Contour connection method for automated identification and classification of landslide deposits. *Comput Geosci* 74:27–38
- Liang T, Knappett JA & Duckett N (2015) Modelling the seismic performance of rooted slopes from individual root-soil interaction to global slope behaviour. *Géotechnique* 65(12):995–1009
- Mahalingam R, Olsen MJ (2015) “Evaluation of the influence of source and spatial resolution of DEMs on derivative products used in landslide mapping.” *Geomat Nat Haz Risk*, 1–21
- Mahalingam R, Olsen MJ & O'Banion MS (2016) Evaluation of landslide susceptibility mapping techniques using lidar-derived conditioning factors (Oregon case study). *Geomat Nat Haz Risk* 7(6):1884–1907
- Melgar D, LeVeque RJ, Dreger DS, Allen RM (2016) Kinematic rupture scenarios and synthetic displacement data: an example application to the Cascadia Subduction Zone. *J Geophys Res Solid Earth* 121(9):6658–6674
- Milledge DG, Griffiths DV, Lane SN, Warburton J (2012) Limits on the validity of infinite length assumptions for modelling shallow landslides. *Earth Surf Process Landf* 37(11):1158–1166
- Milledge DG, Bellugi D, McKean JA, Densmore AL, Dietrich WE (2014) A multidimensional stability model for predicting shallow landslide size and shape across landscapes. *Journal of Geophysical Research: Earth Surface* 119(11):2481–2504
- Miller DJ, Sias J (1998) Deciphering large landslides: linking hydrological, groundwater and slope stability models through GIS. *Hydrol Process* 12(6):923–941
- Ohlmacher GC, Davis JC (2003) Using multiple logistic regression and GIS technology to predict landslide hazard in northeast Kansas, USA. *Eng Geol* 69(3):331–343
- Parker RN, Densmore AL, Rosser NJ, De Michele M, Li Y, Huang R et al (2011) Mass wasting triggered by the 2008 Wenchuan earthquake is greater than orogenic growth. *Nat Geosci* 4(7):449–452
- Petley D (2012) Global patterns of loss of life from landslides. *Geology* 40(10):927–930
- Roering JJ, Schmidt KM, Stock JD, Dietrich WE, Montgomery DR (2003) Shallow landsliding, root reinforcement, and the spatial distribution of trees in the Oregon Coast Range. *Can Geotech J* 40(2):237–253
- Rong Y, Jackson DD, Magistrale H, Goldfinger C (2014) Magnitude limits of subduction zone earthquakes. *Bull Seismol Soc Am* 104(5):2359–2377
- Sakals ME, Sidle RK (2004) A spatial and temporal model of root cohesion in forest soils. *Can J For Res* 34(4):950–958
- Schmidt KM, Roering JJ, Stock JD, Dietrich WE, Montgomery DR, Schaub T (2001) The variability of root cohesion as an influence on shallow landslide susceptibility in the Oregon Coast Range. *Can Geotech J* 38(5):995–1024
- Schuster RL (1996) “Socioeconomic significance of landslides.” *Landslides: investigation and mitigation*. Washington (DC): National Academy Press. Transportation Research Board Special Report, 247, 12–35
- Schwarz M, Lehmann P, Or D (2010) Quantifying lateral root reinforcement in steep slopes—from a bundle of roots to tree stands. *Earth Surf Process Landf* 35(3):354–367
- Seed HB, Martin GR (1966) The seismic coefficient in earth dam design. *Journal of Soil Mechanics & Foundations Div*, 92(Proc. Paper 4824)
- Shukla SK (2013) Generalized analytical expression for dynamic passive earth pressure from $c-\phi$ soil backfills. *Int J Geotech Eng* 7(4):443–446
- Shukla SK (2015) Generalized analytical expression for dynamic active thrust from $c-\phi$ soil backfills. *Int J Geotech Eng* 9(4):416–421
- Sithole G, Vosselman G (2004) Experimental comparison of filter algorithms for bare-earth extraction from airborne laser scanning point clouds. *ISPRS J Photogramm Remote Sens* 59(1):85–101
- Tsai T-L, Yang J-C (2006) Modeling of rainfall-triggered shallow landslide. *Environ Geol* 50(4):525–534
- Umar Z, Pradhan B, Ahmad A, Jebur MN & Tehrani M.S (2014) Earthquake induced landslide susceptibility mapping using an integrated ensemble frequency ratio and logistic regression models in West Sumatera Province, Indonesia. *Catena* 118:124–135
- van Westen C, Terlien MJT (1996) An approach towards deterministic landslide hazard analysis in GIS. A case study from Manizales (Colombia). *Earth Surf Process Landf* 21(9):853–868
- Youssef AM, Pradhan B, Jebur MN & El-Harbi HM (2015) Landslide susceptibility mapping using ensemble bivariate and multivariate statistical models in Fayfa area, Saudi Arabia. *Environ Earth Sci* 73(7):3745–3761

-
- Waldron LJ (1977) The shear resistance of root-permeated homogeneous and stratified soil. *Soil Sci Soc Am J* 41(5):843–849
- Wang Y, Rathje EM (2015) Probabilistic seismic landslide hazard maps including epistemic uncertainty. *Eng Geol* 196:313–324
- Westergaard HM (1933) Water pressures on dams during earthquakes. *Trans ASCE* 98:418–432
- Wu W, Sidle RC (1995) A distributed slope stability model for steep forested basins. *Water Resour Res* 31(8):2097–2110
- Wu TH, McKinnell WP III, Swanston DN (1979) Strength of tree roots and landslides on Prince of Wales Island, Alaska. *Can Geotech J* 16(1):19–33
- Xie M, Esaki T, Cai M (2006) GIS-based implementation of three-dimensional limit equilibrium approach of slope stability. *J Geotech Geoenviron* 132(5):656–660
- Xu C, Xu X, Yao Q, Wang Y (2013) GIS-based bivariate statistical modelling for earthquake-triggered landslides susceptibility mapping related to the 2008 Wenchuan earthquake, China. *Q J Eng Geol Hydrogeol* 46(2):221–236

D. M. Hess

1200 NW Naito Parkway, Suite 180, Portland, OR 97209, USA

B. A. Leshchinsky (✉)

Department of Forest Engineering, Resources and Management,
Oregon State University,
273 Peavy Hall, Corvallis, OR 97331, USA
e-mail: ben.leshchinsky@oregonstate.edu

M. Bunn

School of Civil and Construction Engineering,
Oregon State University,
101 Kearney Hall, Corvallis, OR 97331, USA

H. Benjamin Mason

School of Civil and Construction Engineering,
Oregon State University,
338 Owen Hall, Corvallis, OR 97331, USA

M. J. Olsen

School of Civil and Construction Engineering,
Oregon State University,
313 Owen Hall, Corvallis, OR 97331, USA